

AD-A142 731

A.THEORETICAL ANALYSIS OF PHOTON DRAG DETECTORS(U)
NATIONAL PHYSICAL LAB TEDDINGTON (ENGLAND) DIV OF
ELECTRICAL SCIENCE J G EDWARDS ET AL. MAR 83

1/1

UNCLASSIFIED

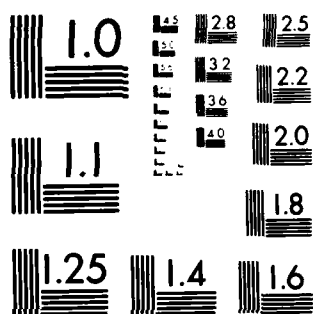
NPL-DES-76

F/G 14/2

NL

		NPL											

END
DATE
FILMED
8 84
DTIC



MICROCOPY RESOLUTION TEST CHART
NATIONAL BUREAU OF STANDARDS-1963-A

AD-A142 731

NPL



National Physical Laboratory

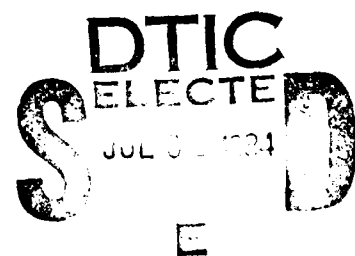
2

DTIC
ELECTE
JUL 03 1984
S E

DTIC FILE COPY

This document is not to be used
for public release, sale, or
distribution in any form.

84 07 02 077



NPL Report DES 76
March 1983

A Theoretical Analysis of Photon Drag
Detectors

by

J.G. EDWARDS and A.G. RODDIE

© Crown copyright 1983

ISSN 0143-7305

National Physical Laboratory
Teddington, Middlesex TW11 0LW, UK

Extracts from this report may be reproduced
provided the source is acknowledged

Approved on behalf of Director, NPL, by Dr O.C. Jones,
Superintendent, Division of Electrical Science

March 1983

NATIONAL PHYSICAL LABORATORY

A Theoretical Analysis of Photon Drag Detectors

by

J.G. EDWARDS and A.G. RODDIE

Division of Electrical Science

Abstract

A theoretical analysis of the spatial response characteristics of photon drag detectors used for the measurement of high power pulses from CO₂ lasers is presented. Details of the model and the numerical methods² employed are described and the results obtained for several electrode configurations together with a comparison of experimental values obtained for a typical commercial device are given.

Accession For	
NTIS GPO&I	
DTIC TAB	
Unannounced	
Justification	
By	
Distribution/	
Availability Codes	
Dist	Avail and/or Special
A-1	



111

CONTENTS

1.	Introduction	1
2.	Principle of operation of photon drag detectors	2
3.	Theoretical model	4
3.1	Numerical technique	5
3.1.1	Boundary conditions	7
3.1.2	Effect of external load	7
3.1.3	Conditions for convergence	9
3.1.4	Accuracy of program	11
3.2	Analytical solution	13
4.	Theoretical and experimental results	15
4.1	Two electrode device	15
4.1.1	Conventional detector	15
4.1.2	Loading conditions	16
4.1.3	Crystal parameters	17
4.1.4	Crystal dimensions	19
4.1.5	Electrode positions and dimensions	20
4.2	Contact resistance	21
4.3	Four electrode detector	22
4.3.1	General properties	22
4.3.2	Improved designs	24
4.4	Quadrant detector	24
5.	Conclusions	26
	References	27
	Table 1	28
	Table 2	29

1. Introduction

Photon drag detectors (References 1,2) are widely used for power and pulse-shape measurement of high-power, pulsed, transversely excited atmospheric pressure (TEA) CO_2 and CO lasers. They have a very fast response time (~ 1 ns), and are linear up to powers close to their damage threshold $\sim 100 \text{ MW/cm}^2$ (Ref.3); in practice, anti-reflection coating damage limits the maximum power density to $\sim 30 \text{ MW/cm}^2$. Unfortunately they have a very low sensitivity, typically 100 mV/MW (Ref.4). No other means are currently available for fast pulse-shape measurements of this type of laser, which is widely used in laser fusion research and range-finders.

Calibrations of the sensitivities of commercially available detectors (manufactured by Rofin Ltd) carried out at NPL have shown their response to be dependent on the position of the laser beam in the device, and this can vary as much as 40% between the centre and the edge.

In this report we describe a theoretical method used to analyse the performance of various designs of detectors by computational techniques. These include the conventional two electrode commercial design, a novel 4 electrode structure designed by us to flatten the spatial variation in the response (Refs.5,6) and a potentially useful 4 quadrant beam centering device. Details of experimental measurements carried out on several detectors made by us are given in a separate paper (Ref.5) although some of the results are given here for comparison with the theory.

2. Principle of operation of photon drag detectors

Only a brief description of the basic theory behind the photon drag effect is presented here. Fuller analyses taking into account the semi-conductor band structure have been given elsewhere (Ref.7) and it is sufficient for our purposes to consider the results obtained by them on the macroscopic scale.

Typically a photon drag detector consists of a cylinder of doped germanium, which is relatively transparent at 10.6 microns, with ring electrodes on the circumference at the ends. This is illustrated diagrammatically in Figure 1. In a standard commercial device, for example the Rofin Ltd. Model 7441, the germanium is usually p-doped to about 10 ohm cm. The laser beam is partially absorbed as it travels through the device and in the process the momentum of the photons is transferred into that of the carriers (mainly the free carriers introduced by doping, although the intrinsic holes and electrons can also make a small contribution). This generates a current flow along the beam, proportional to the laser power density at the point, which then flows back through the bulk of the material. A potential difference is generated between the electrodes and this is measured through an external load resistance. Normally this signal is amplified and viewed on an oscilloscope to display the temporal waveform of the laser pulse. The response time is fast, inherently limited by the relaxation time of the carriers (<10 ps) and the transit time of the laser pulse through the crystal although, in practice, it is mainly determined by the external circuitry, in particular inductance.

Previous analyses of the signal generated (Ref.1) have assumed open circuit conditions (i.e. infinite load) and relatively long, narrow crystals in which the field is uniform in the device. With current

commercial detectors (typically 12.5 mm diameter by 20 mm long) and ring electrodes this analysis is not valid and it is necessary to consider the field distribution within the germanium in order to calculate the sensitivity.

3. Theoretical model

We have carried out a theoretical analysis of the spatial response of detectors under various conditions of illumination and for different electrode configurations. Since the response time of the detector is fast (sub-nanosecond) it is possible to consider a steady-state solution in which a step impulse is incident on the detector. After ~ 1 ns the current densities in the germanium have reached an equilibrium state and the voltage produced between the electrodes is constant. We can therefore ignore transient effects and the build-up of current or carrier mobility and diffusion in the device and assume a CW laser power. An analytical solution to the problem is only possible under special conditions (see Section 3.2). In order to allow arbitrary choices of electrode structures and beam profiles we adopted a numerical approach.

Because of the shape of the device it is convenient to use cylindrical coordinates. Assuming the beam propagates in the positive z direction parallel to the axis the current density generated by the laser is given by

$$J_1(z, r, \theta) = kP_0 F(r, \theta) \exp(-gz) \hat{z} \quad \dots (1)$$

where k is the photon drag coefficient of the material, P_0 is the laser peak power density at the entry face, $F(r, \theta)$ the intensity spatial profile at the entrance position $z = 0$, g the absorption coefficient and \hat{z} the unit vector in the axial direction. Equation 1 expresses the local current flow driven by the laser power. In the above we assume that the ends of the crystal are anti-reflection coated and the material is homogeneous (i.e. g and k are independent of z and r). The electrostatic field $E(z, r, \theta)$ set up by this non-uniform distribution of carriers

produces a current density through the whole of the device

$$J_2(z, r, \theta) = s_0 E(z, r, \theta) \quad \dots (2)$$

where s_0 is the conductivity. Equation 2 merely expresses the normal current flow under the influence of electric fields. The total current density at any point is therefore given by

$$J = J_1 + J_2 \quad \dots (3).$$

Since current continuity, namely $\nabla \cdot J = 0$, must be maintained at every point within the region, the equation which we must solve reduces to

$$\nabla^2 V = - \frac{k P_0 g}{s_0} F(r, \theta) \exp(-gz) \quad \dots (4)$$

which is Poisson's equation where V is the electrostatic potential.

3.1 Numerical technique

If we assume that the laser spatial profile is also cylindrically symmetrical about the crystal axis (a disc or annulus) then we may solve equation (4) in 2 dimensions, which simplifies the problem considerably. In practice we normally take a flat-topped annular power profile, that is constant between two given radial positions and zero elsewhere. By setting up a set of grid points in z and r (see Figure 2) and applying suitable boundary conditions we can use a finite difference approximation to solve the problem numerically using an iterative relaxation process with successive displacement (Ref.8). We used the simplest method where only the four nearest points are considered in calculating the potentials at a grid point. Current flow is calculated from the fields around each grid point and the cross-sectional area

enclosing that region. Each grid point is assumed to have a volume associated with it corresponding to the distance midway to the next point in the axial and radial directions. Grid points at the edges or on electrodes are assumed to lie flush with the surface and the "volume" is calculated appropriately. The external circuit (the load) is taken into account by allowing the current flowing through the electrodes to generate a potential difference across the load and therefore modify the potentials on the electrodes for the succeeding iteration (see below).

In the program an over-relaxation method was used to speed up convergence. The normal successive displacement approach is to calculate the new values of the potentials for the $n+1$ th iteration for each grid point (j,k) using

$$v_{jk}^{n+1} = f(v_{j',k'}^n, \text{Laser Power term}) \quad \dots (5a),$$

where $v_{j',k'}^n$ are the potentials of the four neighbouring points (less at the boundaries) from either the previous iteration set or the current one, since the values are updated (displaced successively) during the iteration cycle. Faster convergence is achieved by using the algorithm

$$v_{jk}^{n+1} = v_{jk}^n + F \cdot (v_{jk}^{n+1} - v_{jk}^n) \quad \dots (5b),$$

where the values v_{jk}^{n+1} on the right side of the equation are calculated from equation 5a. Note that if the constant $F = 1$ the normal successive displacement formula is used. It can be shown (Ref.8) that an optimum value of the over-relaxation factor F can be calculated from the number and sizes of the grids. Using this, although derived for Laplace's equation, it was found that values of F in the range 1.7 to 1.9 gave much faster convergence. If too large a value is used the potentials

tend to oscillate and convergence does not occur.

In a second version of the program assymetry was allowed (using a three-dimensional grid in r, z, θ). Although this requires much larger computer storage and run-times for the same accuracy, it permits the use of localised off-axis beams and also allows segmented electrodes.

3.1.1 Boundary conditions

No current may flow across the boundary of the cylinder either at the ends or on the circumference, unless there is an electrode present. This is allowed for by calculating the total net current flow into each grid "box". This must be zero, even in the case of a region where the laser is generating current. At an electrode, current can flow into or out of the device (see below) but in doing so may alter the potentials of the electrodes, depending on the external load. During one iteration cycle all the electrode potentials are fixed.

3.1.2 Effect of external load

Initially we set up arbitrary values for the potentials within the device and on the electrodes. If, after n iterations, we have a pair of electrodes with potentials of V_1^n and V_2^n , with an external load R_0 connected across them, then we must reset them for the next iteration such that

$$V_2^{n+1} - V_1^{n+1} = I^n R_0 \quad \dots (6)$$

where $I^n = \frac{1}{2} (I_2^n - I_1^n)$ is the mean current flowing into one and out of the other electrode. (I_1^n and I_2^n are calculated from the fields around the electrodes, the conductivity and area.) In general it is found that resetting the potentials in this way is not sufficient to produce a

convergent solution since the two currents can, during early iterations, differ considerably and result in large changes to the potentials. An additional constraint may be applied, namely that the voltages are reset such that the current flowing into the two electrodes are equal and opposite, that is,

$$I_2^{n+1} = - I_1^{n+1} \quad \dots (7a).$$

We may express this in terms of the new electrode potentials and the mean potentials of the grid points adjacent to the electrodes v_1^n and v_2^n , weighted to allow for the grid sizes, (which, along with v_1^n and v_2^n determine the current on the n^{th} iteration), to give

$$v_1^{n+1} + v_2^{n+1} = v_1^n + v_2^n \quad \dots (7b).$$

Solving equations 6 and 7b leads to

$$v_1^{n+1} = \frac{1}{2} (v_1^n + v_2^n - I^n R_0) \quad \dots (8a)$$

and

$$v_2^{n+1} = \frac{1}{2} (v_1^n + v_2^n + I^n R_0) \quad \dots (8b).$$

These formulae give satisfactory results for very low values of load resistance R_0 , but with large ones instability occurs, caused by too rapid changes in the potentials between iterations. A form of under-relaxation is used therefore, the algorithm being the same form as for the standard over-relaxation method, namely

$$v_1^{n+1} = v_1^n + F (v_1^{n+1} - v_1^n) \quad \dots (9)$$

and similarly for v_2^{n+1} . It is clear that this can always satisfy

convergence requirements with a sufficiently small value of F . Similar equations apply to other pairs of electrodes, if present. The value of F was determined by trial and error and found to have typical values of ~ 0.2 and ~ 0.01 for loads R_0 of 50 and 500 ohms respectively although it is dependent on the device dimensions and grid sizes. If the initial values are taken from a previously calculated set for similar electrode positions or beam profile a larger value of F is permissible and speeds up convergence.

The program is also used for calculating the resistance of the device, important for determining the conductivity of the material experimentally. This is done by setting fixed voltages on the electrodes (equivalent to placing a DC voltage across them) and using $F = 0$ in equation 9. By evaluating the current flowing across the electrode-germanium boundary the resistance is calculated.

An additional mode of operation of the program, particularly important when more than two electrodes are employed, is provided for isolated electrodes (rings on the circumference not connected to any external load or to a high resistance). In this case the potentials of the grid points occupied by these electrodes are calculated as though the electrodes are absent and after each iteration they are reset to the mean values. Both connected and isolated electrodes may be combined for any device. The ability to operate the program in this way is also useful for loaded devices as is described later.

3.1.3 Conditions for convergence

The relaxation process is repeated until a suitable stable state is obtained. No restriction is made at any point as to the absolute values of the potentials (a constant may be added to them) and the program will settle to different values depending on the initial values set, although

in practice these are normally zero. Since only differences are required this does not matter.

The number of iterations required depends on the accuracy desired and is a function not only of the number of grid points but also the grid sizes and the electrode and beam dimensions. The criteria used are:

- (a) the change in values of the potentials at all the grid points within the device must tend to zero,
- (b) the currents flowing into or out of the electrode pairs are equal (or agree to within some percentage) and
- (c) the potential differences between the electrode pairs settle to a value.

The most critical of these is (b), especially for large values of load resistance, although the discrepancy can be relatively large (~25%) under some conditions, without significantly affecting the final potentials. For convenience we use another criterion to determine when sufficient iterations have been carried out and allow the program to exit. The two error parameters employed are

$$\text{Error(a)} = \frac{\text{Max}|\delta V_1|}{\text{Mean}|V_1|} \quad \dots (10a)$$

$$\text{Error(b)} = \frac{\sum |\delta V_1|}{\sum |V_1|} \quad \dots (10b)$$

where δV_1 are the changes in the values of V_1 for all the grid points on each iteration ($\text{Max}|\delta V_1|$ is the modulus of the largest change of potential in the region). In general the values of these two parameters are of the same order and the program exits automatically when both of them are less than a specified value typically 10^{-4} .

3.1.4 Accuracy of program

The accuracy of the program is determined mainly by the finite difference approximation to Poisson's equation, and hence the grid sizes and the number of iterations. The program was run for a detector with a single pair of ring electrodes near the ends (the conventional type as detailed in Table 1) with a narrow beam incident on axis, for a range of numbers of grid points axially and radially (M,N), to obtain the potential difference between the electrodes. In each case the specified accuracy, as defined by the error parameters above was the same, 10^{-4} . By running the program for (M,N) values of (21,6) to (101,51) and extrapolating to an infinite number of points the error was found to be $\sim 0.3\%$ in the voltage (for a 101 by 51 grid). Part of this error arises from a variation in the beam diameter imposed by the choice of radial grid size (the response is dependent on radial position as is described below). The effect of the number of iterations was also estimated by plotting the electrode voltages against the inverse number of iterations. Examples of the convergence as a function of iterations and grid sizes are shown in Figure 3. Note that the scales are chosen such that the origin corresponds to an infinite number of iterations or grid points. A relatively coarse grid was used to allow up to 1000 iterations with reasonable run-time. An error of $\sim 0.1\%$ in the voltage was estimated for the above error parameter (10^{-4}), compared with the value on extrapolation to an infinite number of iterations. An overall computational error of $\sim 0.4\%$ (from adding the two above values directly) is considerably less than the experimental errors arising from instrumental errors, imprecise knowledge of the material properties and systematic errors from poor contacting of the ring electrodes. For a given device, however, it is necessary to evaluate the errors using the above methods, since they depend on, among other things, the electrode

dimensions and positions, and the aspect ratio of the crystal. It is not, for example, only the number of grid points that determine the convergence rate, but also the relative grid increments δz and δr . Convergence is much faster if $\delta z > \delta r$. For long thin devices this means a large number of grid points is required if the electrodes are much shorter than the length (the longitudinal grid size must be chosen to allow the correct electrode length), and hence an appreciably greater number of iterations to achieve the same accuracy is necessary. For the conventional device geometry values (M,N) of (51,21) give an estimated accuracy $\sim 1\%$ with 750 iterations, although this number may be reduced if appropriate initial potential values are chosen (eg from previous runs).

As stated above the analysis assumes an annular beam profile. Experimentally, the device was illuminated by a narrow beam at various positions off-axis. It may be shown by superposition theory that the two methods are equivalent - an annular beam can be considered as a number of segments each producing a field distribution in the material. To verify this, the second version of the program was run, with a coarse grid to minimise run-time, to solve the equation in three dimensions with a localised beam. The results obtained were identical as regards the potentials generated on the electrodes for the same beam power although the current distribution in the detector was of course no longer symmetrical.

The effect of the laser beam and the electrodes on the current distribution in the crystal is shown in Figure 4. The potentials were calculated for an annular beam on-axis and a wedge shaped beam off-axis using the two and three dimensional versions of the program respectively. Current lines were derived by considering holes, starting in arbitrary specified positions, allowed to move under the action of

the fields, calculated from the neighbouring potentials, and the laser momentum transfer. Note that, except for lines ending on electrodes - and hence giving rise to the output signal - they form closed loops. Inside the laser beam, although the electric field is such as to drive the current from right to left, the momentum transfer from the laser forces the current in the opposite direction.

3.2 Analytical solution

As a check on the numerical approach we compared the results with those obtained by analytically solving equation 4. This may be done in the imaginary special case of a detector where optically transparent electrodes are positioned on the end faces of the device and the beam occupies the whole region. Equation 4 then takes the one-dimensional form

$$\frac{d^2V}{dz^2} = - \frac{kP_0g}{s_0} \exp(-gz) \quad \dots (11).$$

Integrating this with respect to z gives

$$V_0 = \left(\frac{dV}{dz}\right)_0 L - \frac{kP_0}{s_0g} (\exp(-gL) - 1 + gL) \quad \dots (12),$$

where V_0 is the potential difference between the electrodes, L the length of the devices and $\left(\frac{dV}{dz}\right)_0$ the potential gradient at the left (beam entry) electrode. The current I flowing through the electrode, of cross-sectional area A for a current density J is, using equations 1 - 3, given by

$$I = JA = (kP_0 + s_0E_0) A \quad \dots (13)$$

where P_0 and E_0 are the laser power density and electrostatic field at

the electrode. Since $E_0 = -(\frac{dV}{dz})_0$ and $V_0 = IR_0$, where R_0 is the external load, we can rewrite equation 13 in the form

$$(\frac{dV}{dz})_0 = \frac{k P}{s_0 A} - \frac{V_0}{s_0 R_0 A} \quad \dots (14),$$

where we have replaced the power density P_0 by $\frac{P}{A}$. P is the total laser power which is assumed to be uniform across the device. Substituting this into equation 12 gives

$$V_0 = \frac{k P}{s_0 g A} \frac{(1 - \exp(-gL))}{(1 + \frac{R}{R_0})} \quad \dots (15).$$

where $R = \frac{L}{s_0 A}$ is the resistance of the crystal. For the values given in Table 1, $R = 19.64$ ohms and with $R_0 = 50$ ohms this gives $V_0 = 252.0$ mV. Using the program gives a value of 251.8 mV, in excellent agreement. In the case of infinite load the above equation reduces to the same form as given in Reference 1. Note that if the detector resistance is of the same order as the load (50 ohms), the signal is approximately half the open circuit value and that if the device is reverse terminated by adding a series resistance to make it up to 50 ohm the signal is exactly half the open circuit value (see Section 4.1.2). The behaviour of a detector with ring electrodes is discussed in Chapter 4.

4. Theoretical and experimental results

Using the above numerical techniques we have calculated the sensitivities and the spatial variation of the response of several photon drag detector structures and also the dependence on the material properties of the crystal. These include a standard commercially available device (for which the results are compared with experimental measurements), and a four electrode system, specially designed by us to give uniform response. In addition the effects of poor electrode contacts and a proposed quadrant centering device are described.

4.1 Two electrode device

4.1.1 Conventional detector

Initial calculations were carried out for an existing commercial device on which experimental measurements of the sensitivity had been made. These showed pronounced spatial dependence of sensitivity. The detector, Type 7441 manufactured by Rofin Ltd, has ring electrodes of ~1.5 mm long at each end of the germanium. The properties of the material were not well established but are typically as those given in Table 1, determined from later samples. The signal from the detector was fed into a 50 ohm load and, to avoid reflections, to which the amplifier is sensitive, an additional resistance had been added in series with the crystal to reverse terminate it in 50 ohm. The theoretical and experimental (see Reference 5 for details) sensitivities at 10.6 microns are shown in Figure 5. Because of the lack of accurate figures for the conductivity, photon drag coefficient and electrode dimensions (the electrodes were formed by wires wrapped round the crystal and soldered on, giving a varying thickness) only the relative shapes of the response curves should be considered. The theoretical values were linearly scaled to give agreement in magnitude at the centre. These demonstrate

reasonably good agreement as regard the general form of the curves and emphasise the large variation of the response as a function of the radial position of the laser beam. The discrepancy is probably attributable to variations in the electrode dimensions as later results with improved structures show much better agreement. The fall off in response close to the edge obtained experimentally is caused by the finite beam diameter used. Only part of it is incident on the detector since it overlaps the edge and the effective power absorbed is reduced. In the theoretical computations a very narrow beam is assumed, and the response may be calculated right out to the edge. In principle the program could be modified to allow better comparison with experiment in this region but it was not considered to be necessary. The assymetrical shape of the experimental curve is attributed to variations in the contacting of the electrodes to the crystal and a more detailed analysis of the effects of this is considered in Section 4.2.

4.1.2 Loading conditions

Equation 15 shows that for a device of resistance R generating an open circuit voltage V_{oc} , the signal produced into a resistive load R_0 is given by V_L where

$$V_L = \frac{V_{oc}}{(1 + \frac{R}{R_0})} \quad \dots (16).$$

Since it is normal practise to reverse terminate detectors, to avoid reflections which affect amplifier response, the resistance of the device must be known before the total load resistance across the device can be calculated and the reponse of it determined. This is inconvenient if parameters such as the electrode sizes or positions are being varied and consequently the resistance changes. However, it may be easily shown that with reverse termination and feeding into the same load (50 ohms)

the output signal is exactly half V_{oc} irrespective of the device resistance. Although it is not possible to show mathematically that Equation 16 also holds for a detector with ring electrodes, the effect of any load across the device is to act as a shunt. It is therefore simpler to carry out all calculations under the open circuit condition (and speeds up the rate of convergence slightly). The signal obtained with any other load or reverse termination can then be evaluated using Equation 16.

4.1.3 Crystal parameters

In attempting to compare theoretical and experimental results a difficulty arises through lack of knowledge of some of the germanium crystal parameters. In particular the conductivity and photon drag coefficient are not normally well known; the absorption coefficient can be determined experimentally. The resistance of the detector can, however, be measured and compared with the resistance calculated and the conductivity may therefore be determined. The photon drag coefficient is less important in that the results obtained can be scaled linearly for comparison of relative response. The three parameters, conductivity, absorption and photon drag coefficients are interdependent; from a simplistic physical model one can consider that high doping of the crystal leads to high conductivity, greater absorption of photons and higher transfer of momentum to the carriers. The precise details and the relationship between them is not considered here but fuller descriptions have been given elsewhere (Refs.1,10). It is therefore sufficient to know the conductivity (or resistivity) of the material accurately to determine the absolute sensitivity of a device. For convenience the relationships (Ref.5) are reproduced in Figure 6(a). It is also interesting to note how the overall sensitivity behaves as a function of the resistivity. This is shown in Figure 6(b) which has been obtained

using the relationship between the parameters and Equation 15. Note that in general low conductivity material is to be preferred.

It is, however, also useful to know the way in which the sensitivity scales with the individual parameters since then any calculations can be scaled. For the simple case of a detector with electrodes on the end faces (referred to as the end-electrode device) the dependence of the signal on the crystal conductivity, photon-drag and absorption coefficients is given by Equation 15. It is clear that for ring electrodes the scaling will be the same, that is linear, for the conductivity and photon-drag coefficient. However, the absorption coefficient alters the current generated in a non-linear manner (exponentially) which affects its distribution in the crystal and hence the signal measured on the electrodes. We have calculated the response and axial variation for two ring electrodes 2 mm long. The behaviour is shown in Figure 7. The axial signal is plotted against both the absorption coefficient and the parameter $\frac{(1 - \exp(-gL))}{g}$, for which one expects a linear relationship in the case of the end-electrode device. Note that the line is almost straight implying that scaling is approximately the same as for an end-electrode detector with only a small deviation over the range. This is sufficiently small to enable us to use the end-electrode calculation to obtain preliminary estimates for design purposes and scaling the results. For absolute response a fuller analysis is required. The non-uniformity of response, defined here as the signal close to the edge divided by the axial value increases with the absorption coefficient; this might be expected since the signal is absorbed closer to the input end of the detector and the current produced will have a proportionally greater radial to axial distribution.

4.1.4 Crystal dimensions

The dimensions assumed up till now, have been those typical of a Rofin 7441 detector. In practice, however, we must select these according to the desired application. Detectors may be used in two ways - as in-line monitors, in which case a high transmission is required (typically 70%) commensurate with adequate sensitivity, and as power meters where most of the radiation may be absorbed. This places conditions on the length of the detector (assuming a restricted availability of choice in the crystal resistivity) and its radius. For high power use a large diameter beam must be used to avoid damage to the germanium.

Since it has been shown above, from the use of Equation 15, that the voltage generated by an end-electrode detector predicts the general form of the behaviour for ring structures, although not, of course, for response flatness, it is useful to apply it and compare the sensitivity as a function of the crystal length and area. In terms of these two parameters the signal produced V is

$$V \propto F_1 = \frac{(1 - \exp(-gL))}{A} \quad \dots (17).$$

The behaviour can be shown by plotting the voltages obtained for ring electrodes against the parameter F_1 . We have calculated the axial and off-axis open circuit signals for two samples of the same material, lengths 20 and 50 mm, with different radii. The electrodes for the two lengths are 1.75 and 2.5 mm long respectively, of ring structure on the circumference at the ends. The axial voltages against F_1 are shown in Figure 8(a), together with the values calculated from Equation 15. The agreement is sufficiently close to enable useful design decisions to be made. An alternative parameter to use is the "Aspect ratio", defined

here as $\frac{L}{A}$. In terms of physical dimensions this is more meaningful and although no simple relationship can be expected the relationship is similar (Fig.8(b)). Note that from Equation 17 if $gL \ll 1$ (low absorption) the end-electrode signal is inversely proportional to the area and hence the aspect ratio for a given length.

The aspect ratio also affects the reponse as a function of beam position. The signal relative to the axial value is plotted as a function of the relative radial position (that is the beam position divided by the cylinder radius) in Figure 9(a). The behaviour can be seen more clearly by considering the non-linearity as a function of the inverse aspect ratio. This is shown in Figure 9(b) where the relative signal V_r is defined as the ratio of the signal for the beam at 50 % of the cylinder radius to that on axis. As can be seen, the reponse is flatter for longer devices. For a given crystal length therefore, the flatness of response is better for devices with smaller radii as is the overall sensitivity. Where possible the smallest radius should be used, consistent with the laser beam radius and damage threshold requirements.

4.1.5 Electrode positions and dimensions

We calculated the reponse properties of a detector 20 mm long by 12.5 mm diameter with various combinations of electrode positions and lengths, to determine the effect on sensitivity and flatness of response. The knowledge of the behaviour as these are varied is important for comparison with experiment, in addition to determining the optimal configuration, since it is difficult to measure the effective widths of electrodes accurately.

Figure 10(a) shows that as the electrodes (1.2 mm long) are moved in towards the centre the axial (and consequently total) signal is reduced. In addition the ratio of the off-axis (at 75% of the crystal radius) to

the axial signal above) is seen to decrease similarly, implying that by moving the electrodes away from the ends an improvement in profile flatness is obtained, although at a cost in sensitivity as shown in Figure 10(b).

A similar behaviour occurs as the lengths of the electrodes, which extend to the ends of the crystal, are altered, and this is shown in Figure 11. The results are similar to those above, (short electrodes at different positions) which is to be expected since the parts of the electrodes nearer to the centre have a dominant effect on the response. The program is less accurate in calculating the behaviour if the electrodes become too close together (at the centre) because of the large differences in the fields near the electrodes between the ends and centre. Decreasing the grid sizes improves the accuracy (at the expense of computer time) although for practical purposes this is not necessary. An alternative way to increase the accuracy would be to use a 9 point algorithm (the 8 points nearest the grid point being calculated) instead of a 5 point one but again this is not important for our purposes.

4.2 Contact resistance

In calibration of photon drag detectors it is often found that although the sensitivity is much greater at the edge the response is not symmetrical about the axis (Fig 5). A possible explanation for this is poor contacting of the electrodes to the germanium, with electrical contact being achieved only over part of the circumference. To investigate this we used the three dimensional version of the program to calculate the response as a function of beam position where the electrodes consisted of segments of rings. For simplicity we assumed that both electrodes consisted of partial rings, in contact with approximately 60% of the circumference only. Both electrodes covered the

same angular region of the device. The results are shown in contour form in Figure 12(a). These contours were calculated using a standard routine (Ref.9), modified slightly to reduce the weightings placed on regions close to data points, and they display the typical form encountered experimentally. Figure 12(b) shows the profile along the x-axis. In practice, real detectors are liable to show more random variations, because of irregular contacts.

4.3 Four electrode detector

As shown above, the two-electrode structure is much more sensitive at the edge than in the centre although the flatness may be improved by shifting the electrodes closer together. We felt that by using a pair of signal electrodes closer together and applying a shunt resistance across a pair at the end the response could be flattened.

4.3.1 General properties

We have, therefore, designed a four-electrode device (see Figure 13) in which the two outer ones are connected together via a variable resistor and the signal is generated between the inner pair. The outer electrodes are 1.5 mm long and the inner pair 1.4 mm centred 3.8 mm from the ends. The variation of response (open-circuit voltage) determined theoretically, as a function of beam position, is shown for a range of values of the outer resistance. (The crystal parameters are as before.) As can be seen, it is possible, by suitable outer loading to achieve a response flat to $\sim 4\%$ over the whole area. This is within the normal calibration accuracy of $\pm 5\%$ absolute, $\pm 2\%$ relative. The sensitivity attained for this uniformity is higher than can be obtained using one pair of electrodes which would have to be positioned closer together.

Figure 14 shows the theoretical and experimentally measured

sensitivities for a device which we produced (Ref.5). The calculations were based on accurately measured electrode lengths and positions together with the crystal parameters. These curves are for a signal load of 50 ohms. The resistance across the inner pair (the device resistance) was 12.5 ohms. In order to obtain the absolute values of the crystal parameters for comparison both the conductivity and absorption coefficient were measured. The photon drag coefficient was obtained by scaling the value in the theoretical prediction to the experiment to give a fit for the axial sensitivity measured across the outer electrodes with the inner pair isolated. The good agreement in profile and in the magnitude of the signals measured across the inner pair demonstrate the excellent correspondence between the theory and experiment. The conductivity was evaluated theoretically by assuming an arbitrary value and applying a fixed voltage across the outer pair of electrodes and calculating the voltages on the isolated central pair. The potential difference could thus be calculated across the inner pair for a known current flow through the crystal. By measuring this experimentally the voltages could be compared and the conductivity derived. The advantage of this four terminal method is to eliminate any errors that could be caused by contact potentials between the electrodes and crystal (although it cannot determine the effects of any non-uniformities in the material). Using this value for the conductivity and repeating this 4 - terminal measurement, theoretically and experimentally, between all combinations of electrodes with the contact resistances at all electrodes can be calculated. It was found that with our newly developed method of vacuum deposition of the electrodes (details in Ref.5), there was negligible contact resistance - to within the errors involved.

4.3.2 Improved designs

The effect of the conductivity on the sensitivity was described in Section 4.1.3, in which the advantage of low conductivity germanium was shown. We have therefore designed two new detectors to be used as in-line beam monitors with approximately 75 % transmission with diameters of 12.5 mm and 22 mm for handling different laser powers. The relevant crystal parameters, electrode positions and theoretical performances are given in Table 2. It is interesting to note that for the narrow version little improvement is achieved by using 4 electrodes and satisfactory uniformity of response can be obtained by placing the electrodes only 5 mm from the ends. In practice, however, it is useful to have the additional electrodes for resistance measurement. These devices are currently under construction.

4.4 Quadrant detector

A possible modification to the conventional design, making use of the non-uniformity with beam position, is to segment the electrodes into four sections to produce a "quadrant" detector which can be used for beam centering at 10.6 microns (Fig. 15(a)). By measuring the potential difference between corresponding pairs of segments (with equal loads of 50 ohms) and taking the difference voltages in the X and Y directions a signal is generated if the beam is off-axis (Fig. 15(b)). A difference voltage of ~ 1 mV (a 5% variation) is produced by a 1 mm displacement of the 1 MW beam in either direction, a signal well within measurement capabilities. The calculations have been carried out for the original crystal and dimensions and an improvement on the differential response could be obtained by altering the aspect ratio (shortening the crystal) and crystal conductivity to improve the sensitivity. The limit to the application of this approach and the usefulness are determined mainly by

the difficulties of measuring small signals in the electrically noisy environment of TEA lasers.

It should, however, be noted that the signal varies non-linearly with beam displacement. In addition, the form of relationship is more complicated if the shift is at an angle to the x or y axes, resulting in "cross-talk" between the signals. While this is not necessarily important for well-behaved uniform (or symmetrical) beam profiles, the presence of non-uniformities (eg "hot spots") can give erroneous results for the position of the centroid of the beam. For this reason, the use of a slower linear detector, for example a pyroelectric system, would be more useful.

5. Conclusions

We have shown that the numerical approach developed to calculate the spatial response of photon drag detectors gives results in very good agreement with experiment. This has enabled us to develop various electrode configurations which allow either flattening of the response without too great a loss in sensitivity, or a potentially useful beam alignment method. The importance of achieving good uniform electrical contact between the ring electrodes and the crystal has also been demonstrated and is essential if reliable accurate power measurement with variable size laser beams is required.

Acknowledgements

We wish to thank Mr.P.A.Smith, Division of Electrical Science, for carrying out the experimental measurements and producing the new improved detectors.

References

- 1 A.F.Gibson, M.F.Kimmit and A.C.Walker, Photon drag in germanium, Appl.Phys.Lett., 17 (1970), 75
- 2 A.M.Danishevskii, A.A.Kastalskii, S.M.Ryokin and I.D.Yaroshatskii, Dragging effect of free carriers by photons in direct intraband transitions in semiconductors, Sov.Phys., JETP, 31 (1970), 292
- 3 T.Kamibayashi, S.Yonemochi and T.Miyakawa, Superlinear dependence of photon drag voltage on incident power density, Appl.Phys.Lett., 22 (1973), 119
- 4 M.F.Kimmit, D.C.Tyte and M.J.Wright, Photon drag radiation monitors for use with pulsed CO₂ lasers, J.Phys.E: Sci.Instrum., 5, (1972), 239
- 5 J.G.Edwards, A.G.Roddie and P.A.Smith, to be published in J.Phys.E: Sci.Instrum. (May 1983)
- 6 J.G.Edwards and A.G.Roddie, UK Patent Application No 8125376, (1981).
- 7 A.F.Gibson and S.Montasser, A theoretical description of the photon-drag spectrum of p-type germanium, J.Phys.C: Solid State Phys., 8 (1975), 3147
- 8 C.Weber, Analogue and digital methods for investigating electron-optical systems, Philips Res. Report, Suppl.6 (1967),23
- 9 K.J.Falconer, A general purpose algorithm for contouring over scattered data points, NPL Report NAC 6, (1971)
- 10 P.J.Bishop and A.F.Gibson, Absorption coefficient of germanium at 10.6 μm , Appl. Optics, 12 (1971),2549

Table 1

Typical crystal parameters and dimensions of 2 electrode detector

Crystal length	L	20.0 mm
Crystal radius	r_c	6.25 mm
Cross-sectional area	A	1.227 cm ²
Electrode lengths ⁽¹⁾	l	1.5 mm
Device resistance ⁽²⁾	R_c	20.6 ohms
External load	R_0	50 ohms
Conductivity ⁽³⁾	s_0	8.3 ohm ⁻¹ m ⁻¹
Photon drag coefficient ⁽⁴⁾	k	22.3 10 ⁻⁹ A/W
Absorption coefficient ⁽⁵⁾	g	23.0 m ⁻¹
Laser power ⁽⁶⁾	P	1.0 MW

Notes

- (1) Electrodes positioned on circumference at the ends of the crystal.
- (2) Calculated numerically from the detector parameters.
- (3) Calculated by matching the experimentally measured and calculated values for this device.
- (4) Value found by scaling theoretical sensitivities to experimental ones.
- (5) Measured experimentally at 10.6 microns.
- (6) A constant value for the total power was used and the power density P_0 (dependent on the beam profile) calculated at run-time.

Table 2

Parameters and predicted responses of 4 electrode detectors

NPL device		I	II	III
Crystal length	mm	30	30	20
Crystal radius	mm	11.0	6.25	6.25
Inner electrode position	mm	7.5	5.5	3.8
Conductivity	$\Omega^{-1} \text{m}^{-1}$	4.0	4.0	10.0
Resistivity	$\Omega \text{ cm}$	25.0	25.0	10.0
Photon drag coefficient	nA/W	11.1	11.1	18.6
Absorption coefficient	m^{-1}	9.8	9.8	19.0
Transmission	%	75	75	68
Resistance ⁽²⁾	Ω	13.6	45.0	10.0
Outer load ⁽³⁾	Ω	50	-	50
Predicted sensitivity	mV/MW	77	370	103 (4) 185 (5)

Notes

- (1) Distance between centre of electrode and crystal end.
- (2) Between inner electrodes with appropriate outer load.
- (3) Resistive load connected across outer pair of electrodes to give flattest response.
- (4) Across the inner electrodes with an infinite impedance; (ie open-circuit signal) for a narrow on-axis beam.
- (5) Open-circuit voltage across the outer pair of electrodes with the inner pair isolated - this is approximately the same as for a two electrode detector of the same dimensions.

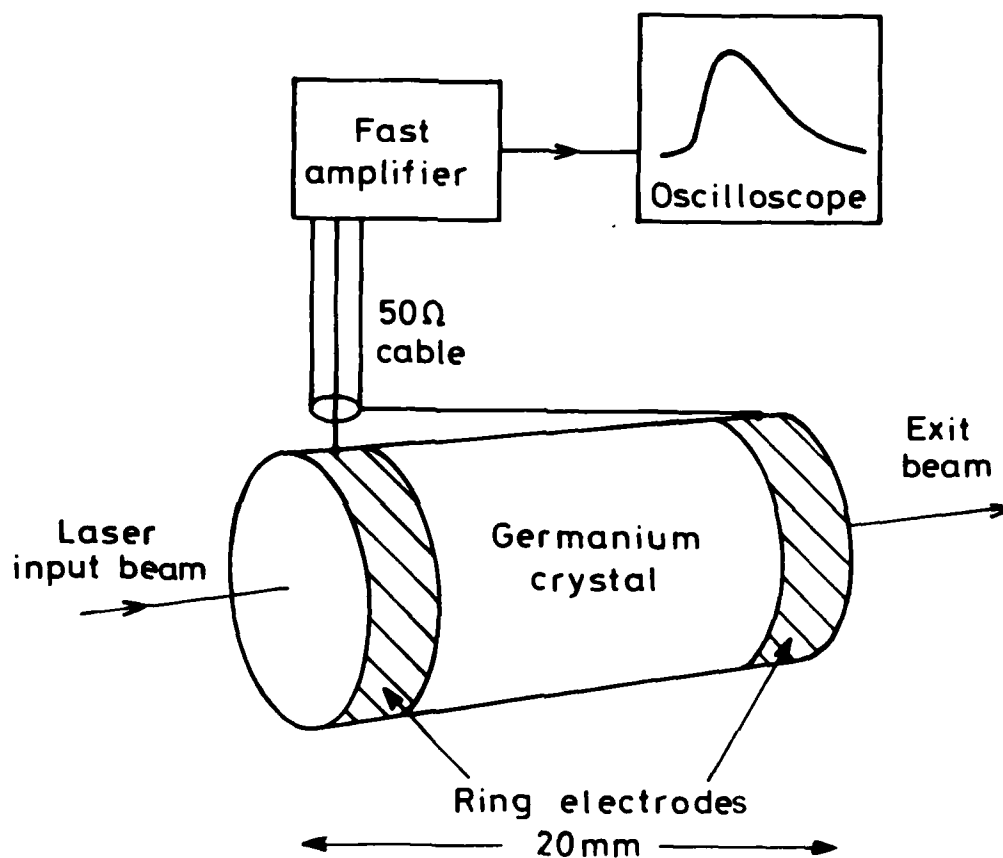


Fig.1 Schematic diagram of a typical two-electrode photon drag detector.

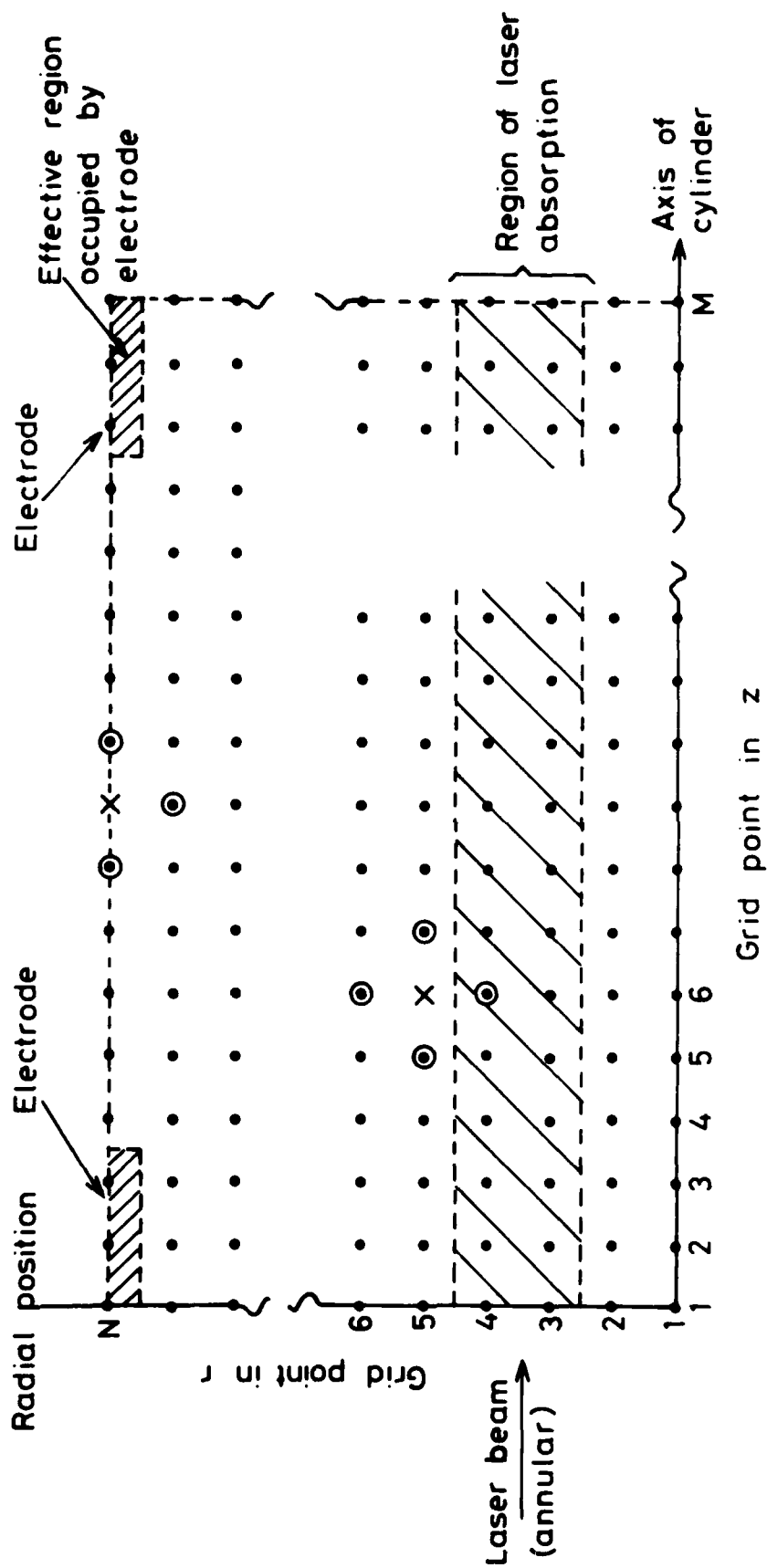


Fig.2 Grid structure used for numerical computation of electrode potentials and device resistance. The potentials at points \otimes are calculated from the neighbouring ones \odot .

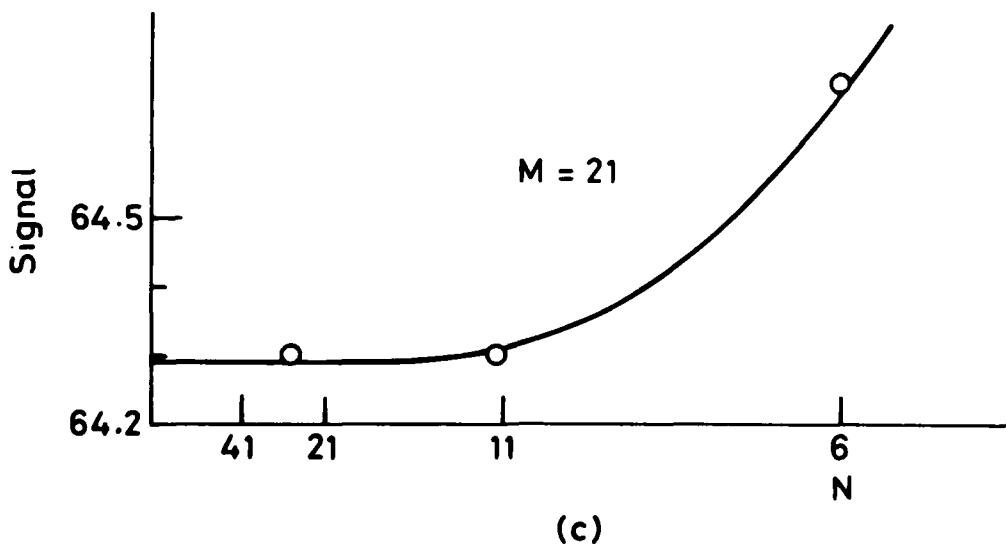
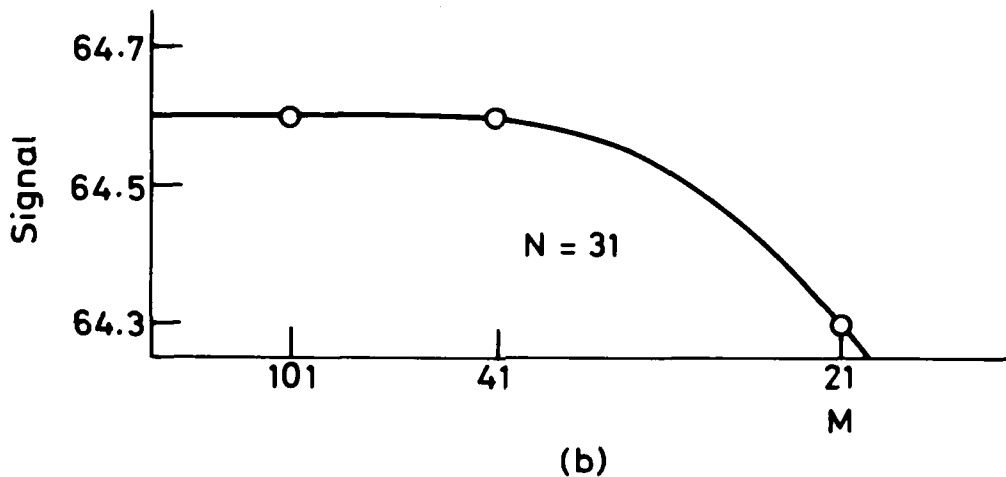
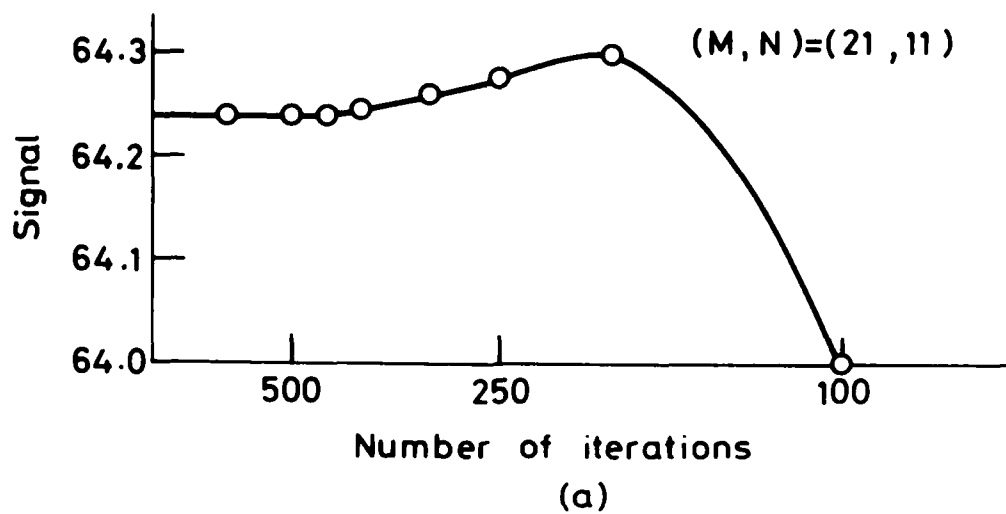


Fig.3 Convergence of the detector signal (electrode potential difference) as a function of: (a) the number of iterations for a fixed grid size ; the number of grid points in the axial (b) and radial (c) directions. In (b) and (c) the error parameter was the same for all sets.

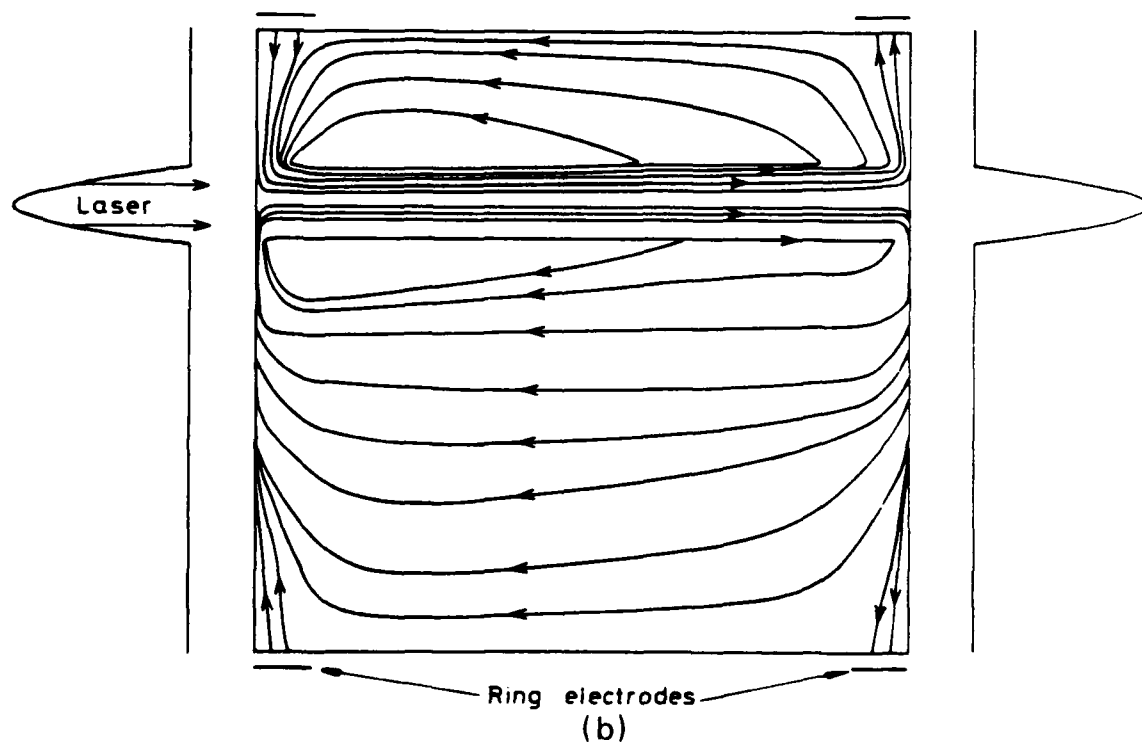
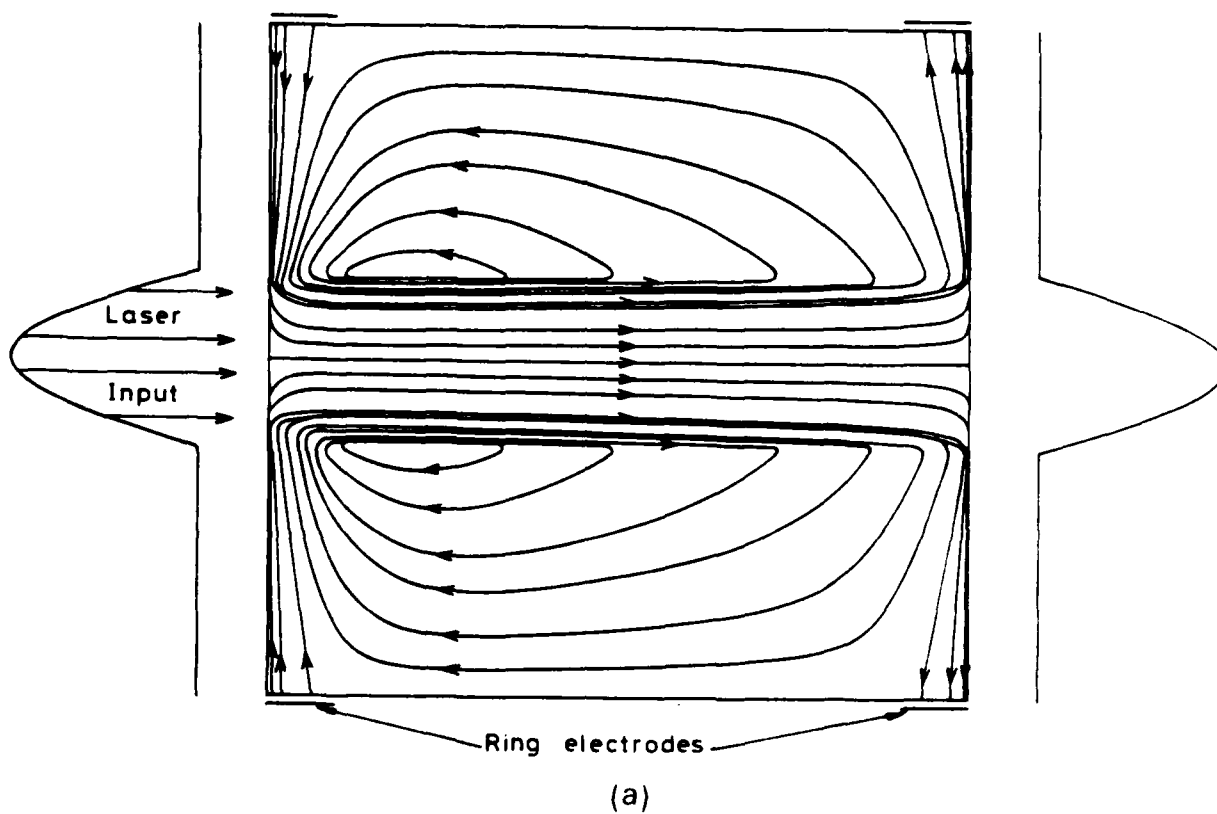


Fig.4 Typical current loops for a two electrode detector with 2.0 mm electrodes loaded by 50Ω . (a) Central beam of pattern shown and (b) narrow off-axis beam.

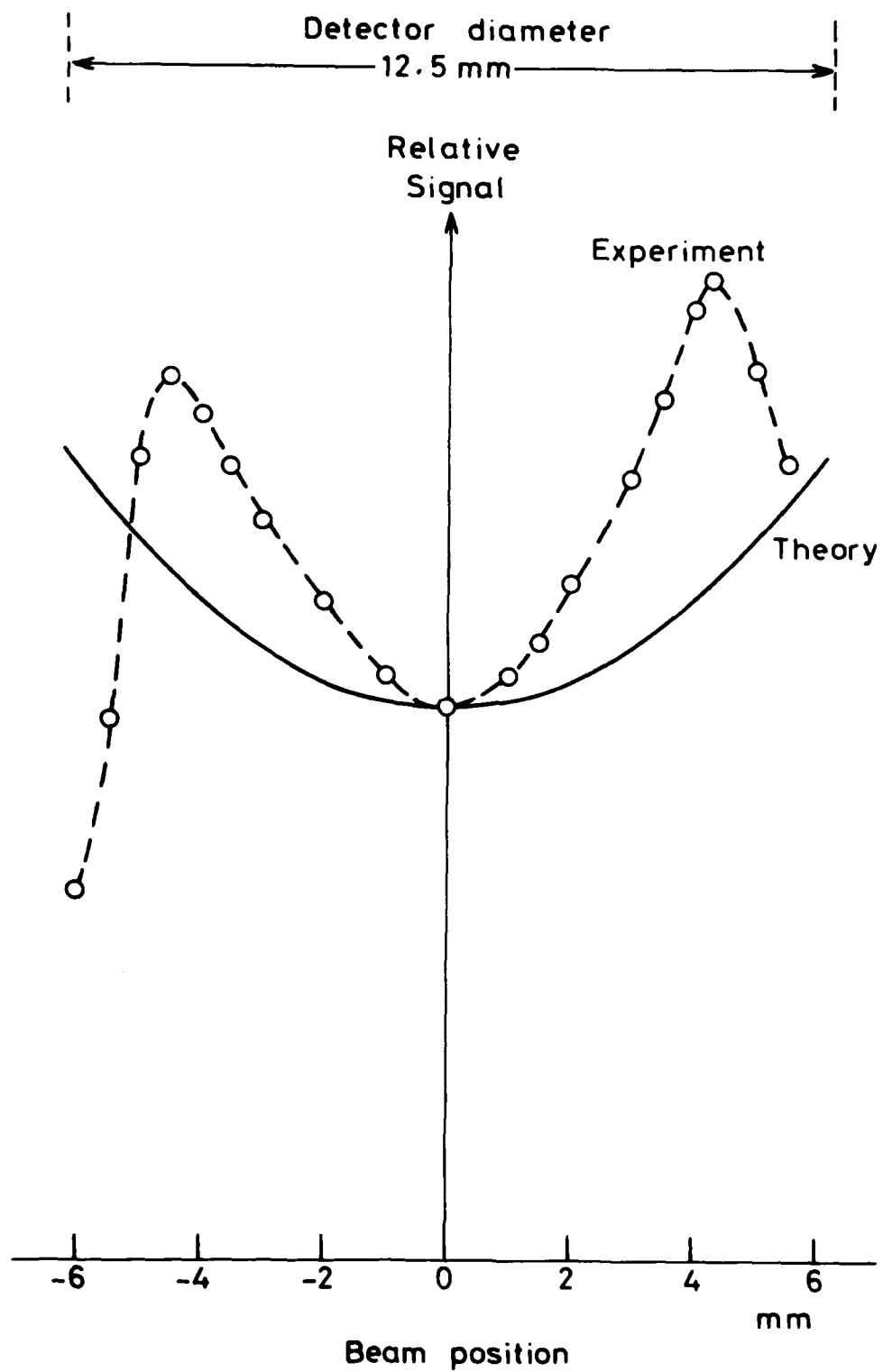


Fig.5 Experimental and theoretical spatial response of a Rofin 7441 detector. The signals have been linearly scaled to agree on axis.

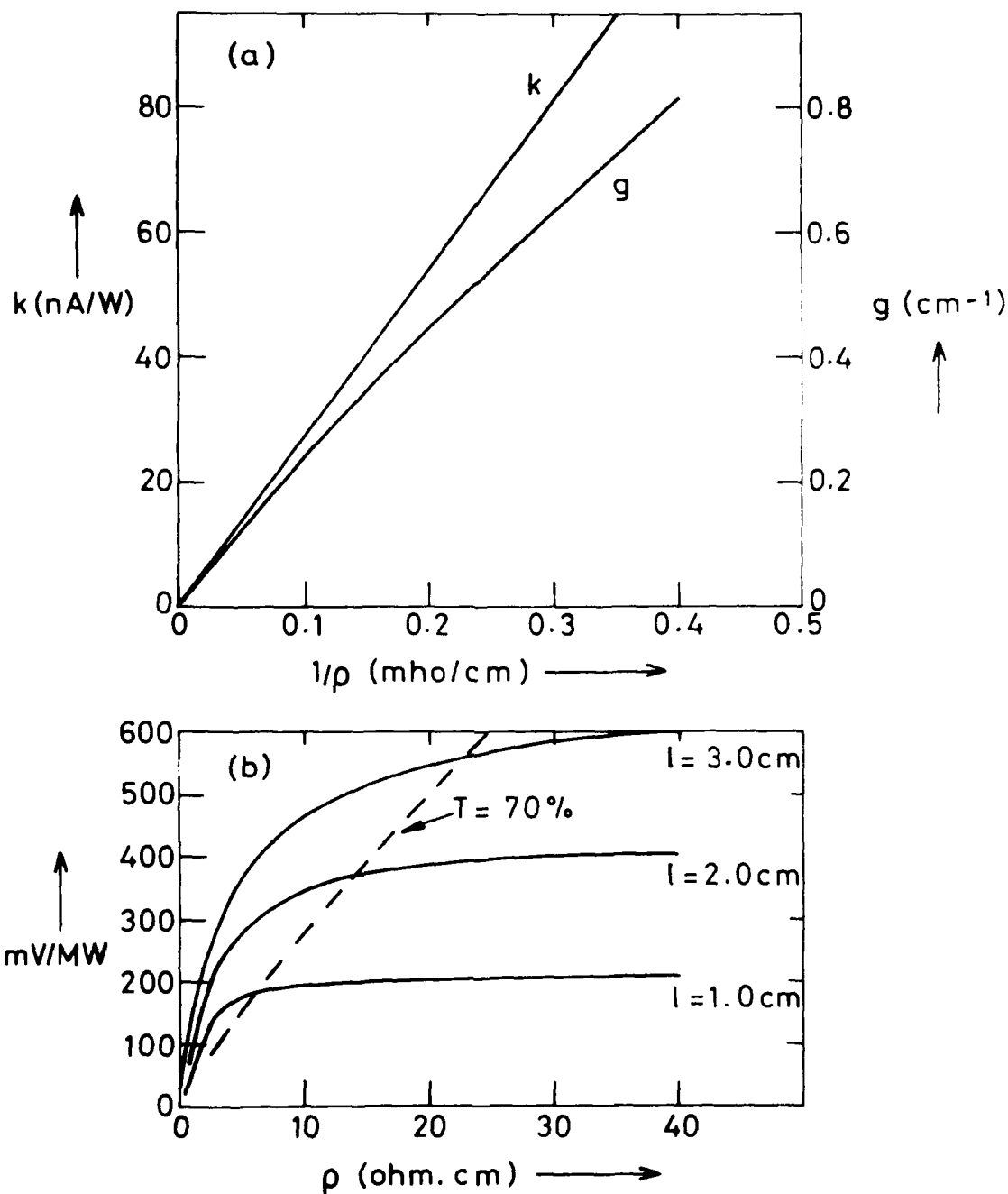


Fig.6 (a) Dependence of the photon drag coefficient k and the absorption coefficient g on the conductivity ($\sigma = 1/\rho$); (b) the sensitivity of an end-electrode detector as a function of the material resistivity (calculated from Equation 15).

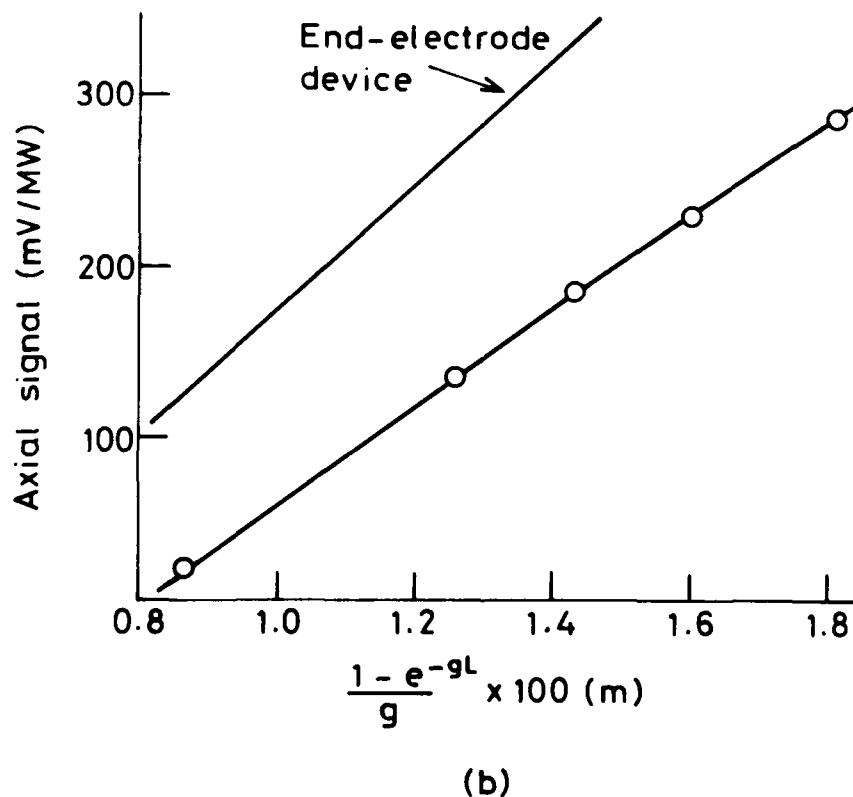
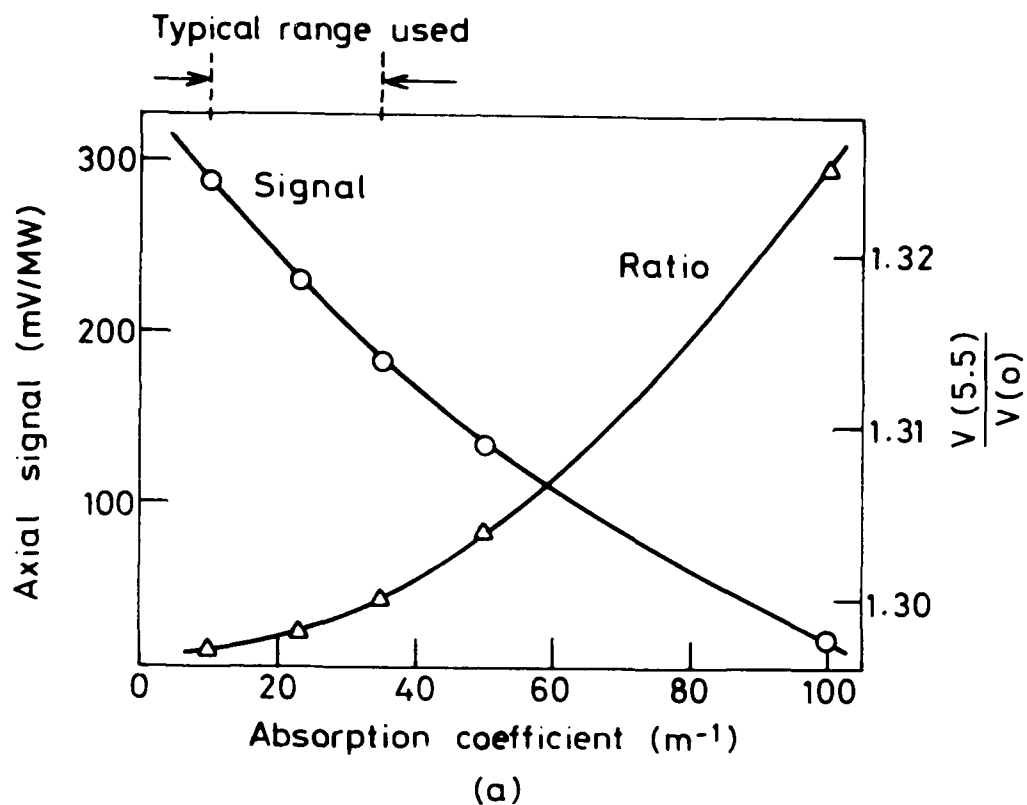


Fig. 7 (a) Variation of the axial signal and the flatness of response $\frac{V(r=5.5)}{V(r=0)}$ with absorption coefficient; (b) axial signal as a function of $\frac{(1 - e^{-gL})}{g}$ (see text) and the corresponding dependence for the end electrode case.

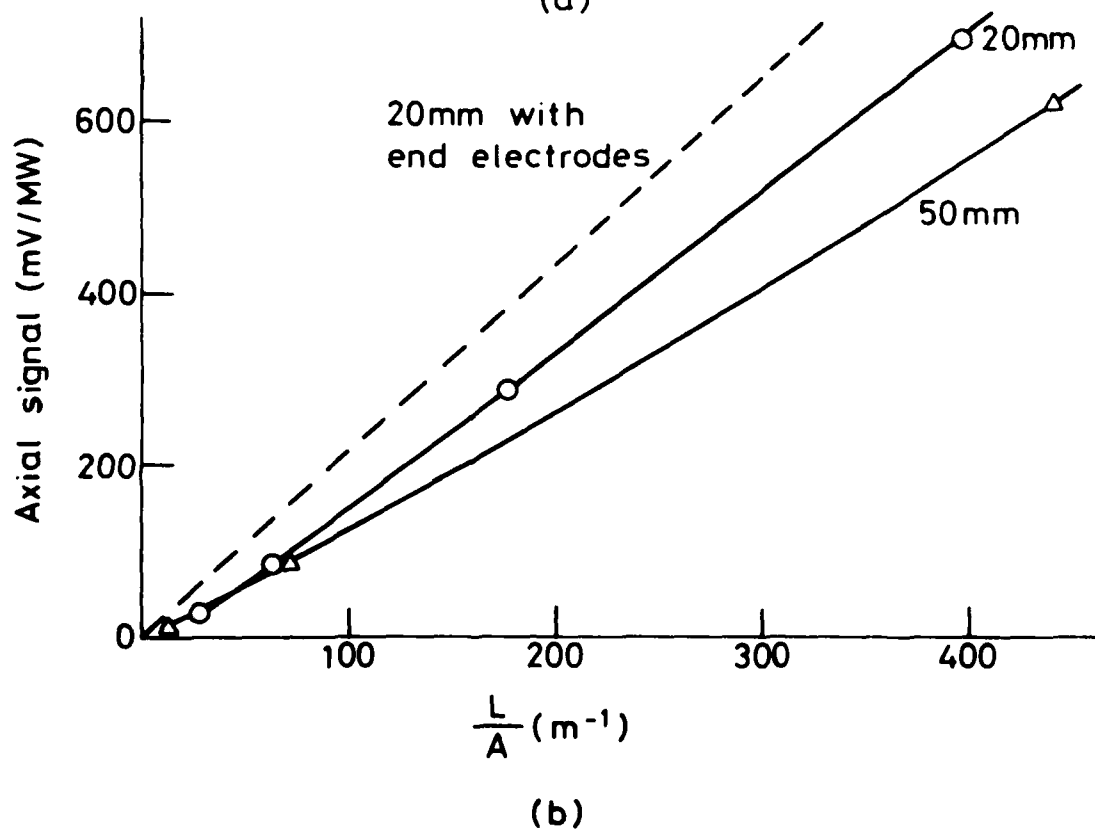
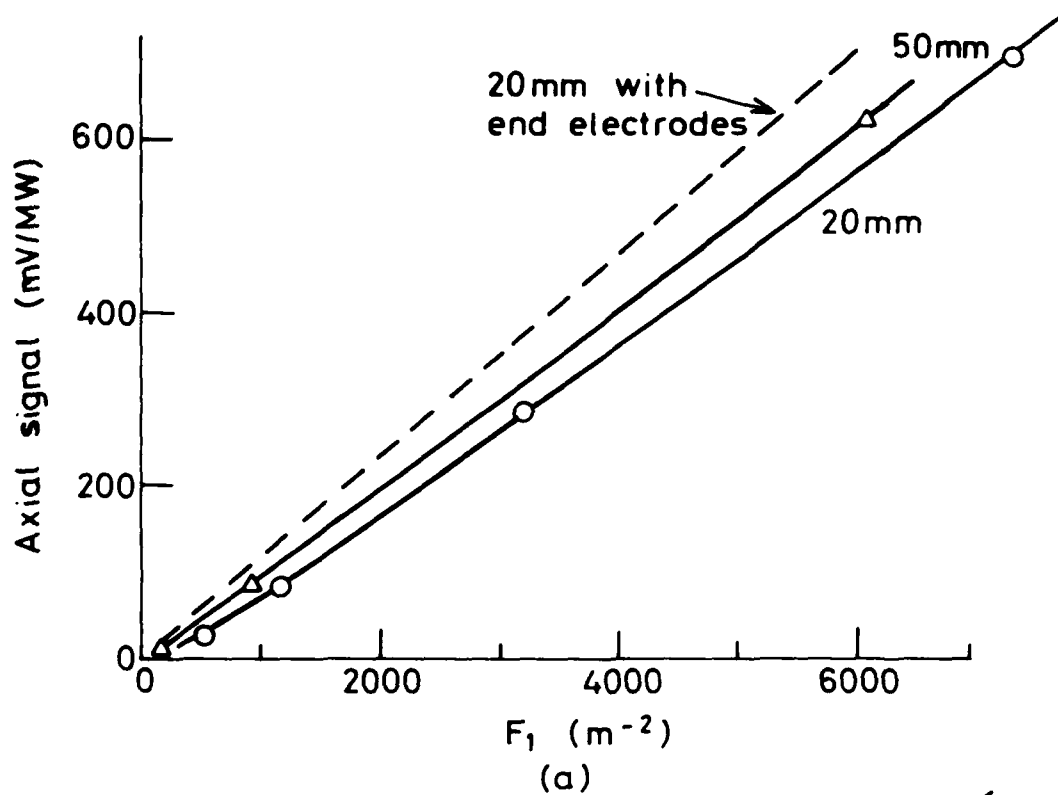
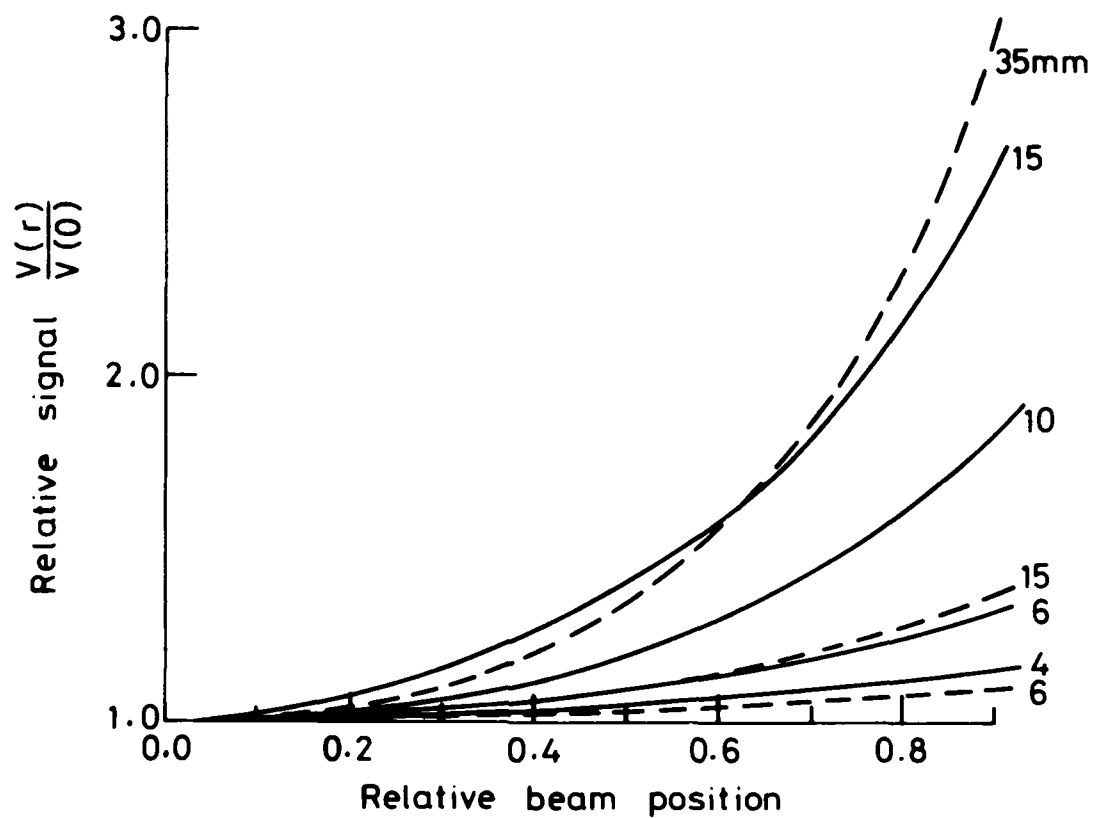
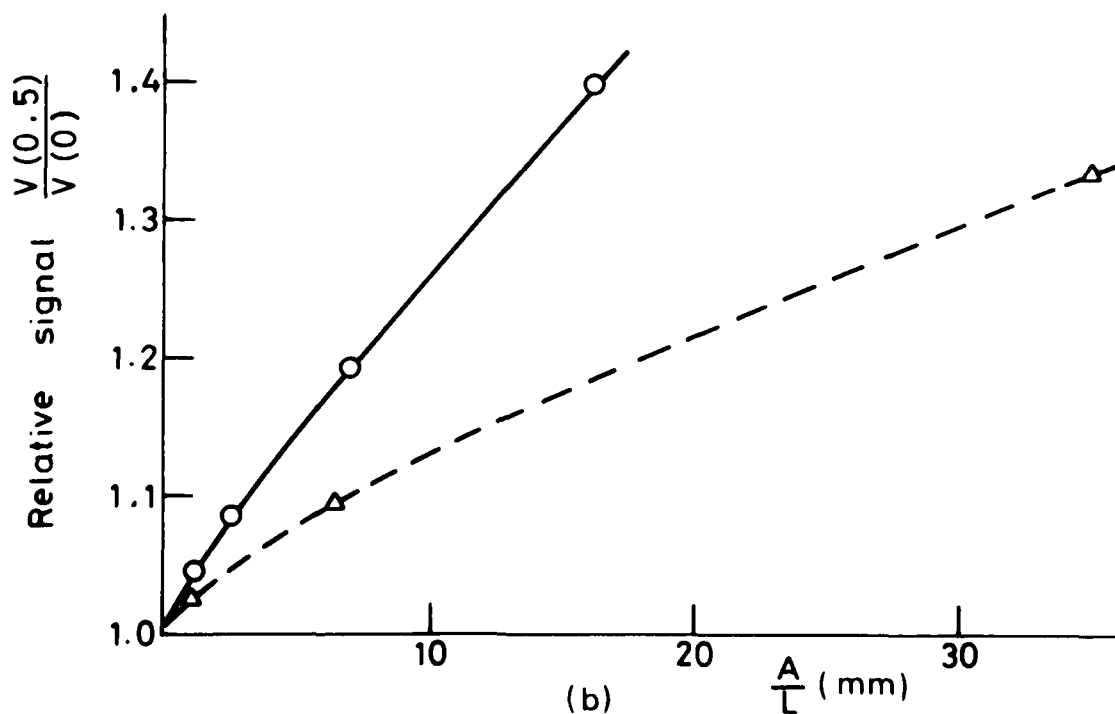


Fig.8 Variation of detector signal with aspect ratio described by
 (a) the parameter F_1 (aspect ratio weighted by absorption factor)
 and (b) the aspect ratio itself. Crystal lengths 20 and 50 mm.



(a)



(b)

Fig.9 Effect of the aspect ratio on the spatial response for 20 mm (solid lines) and 50 mm (dashed lines) long detectors; (a) as a function of the relative beam position from the axis (radius of device = 1.0) and (b) the ratio of the signal at 50% of the radius to the axial signal as a function of the inverse aspect ratio.

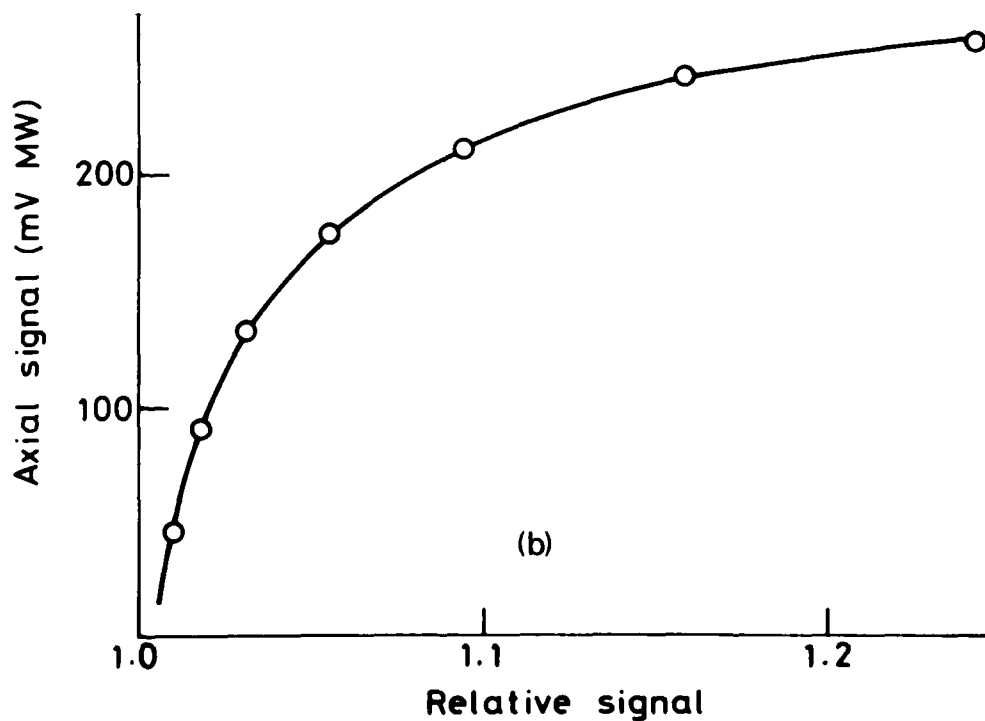
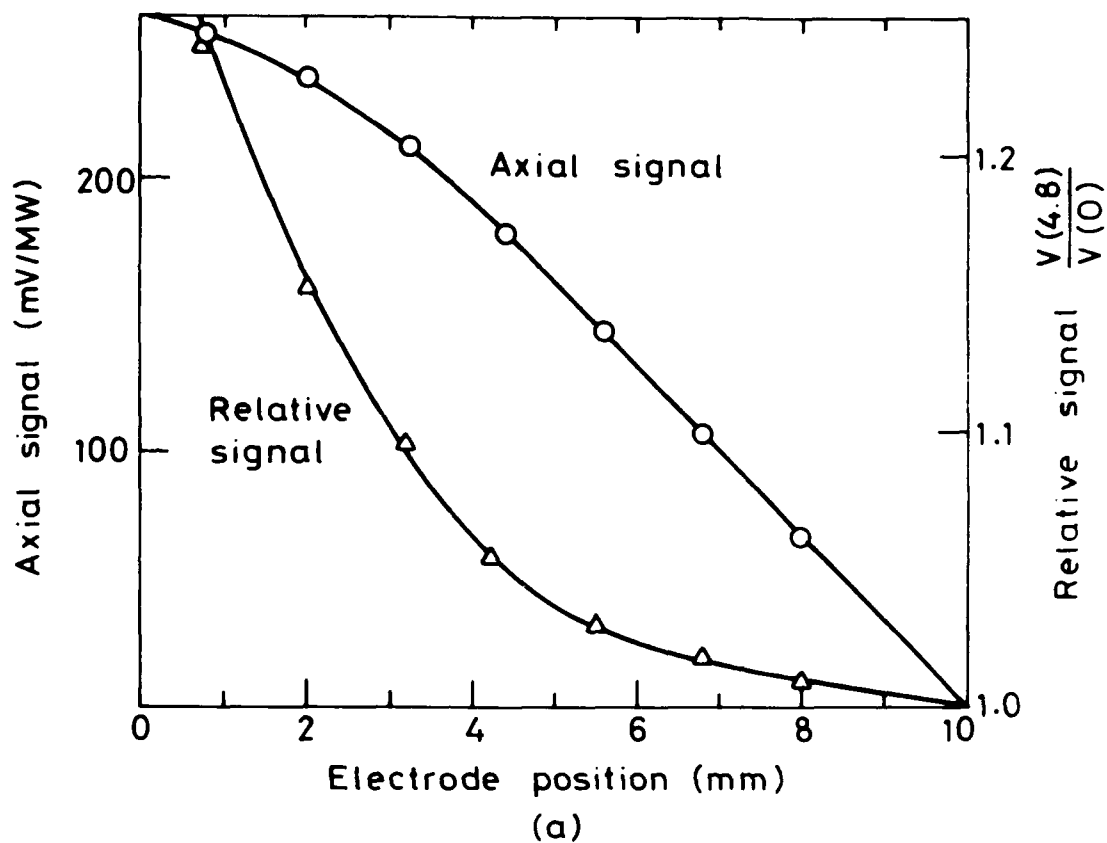
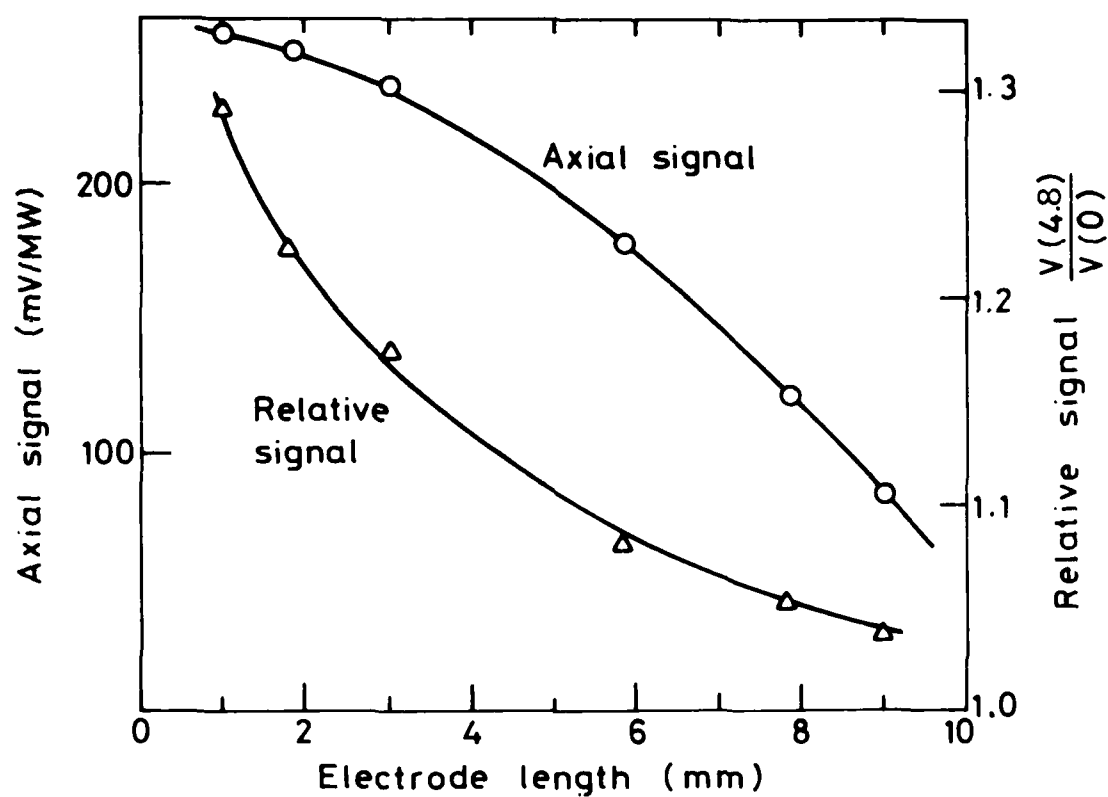
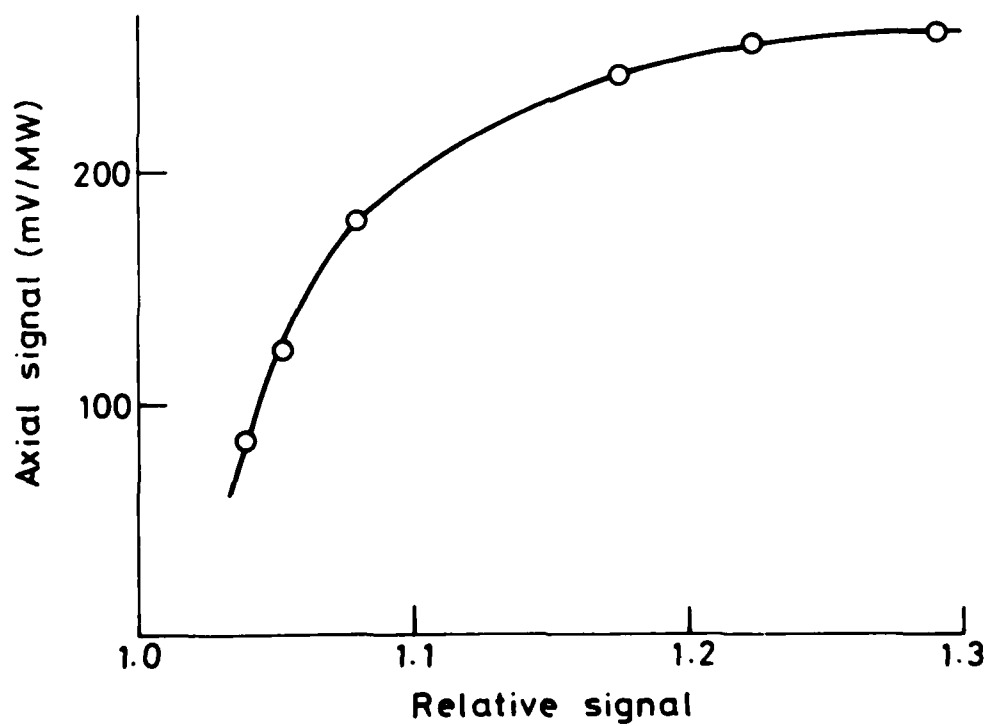


Fig.10 (a) Signal and flatness of response as the positions of the electrodes (1.2 mm long) are moved in symmetrically from the ends of the crystal. The relative signal is defined as the ratio of that at 75% of the radius to the axial value. (b) The above values plotted to demonstrate the trade-off in sensitivity against flatness.



(a)



(b)

Fig.11 (a) Signal and flatness of response as a function of the length of the electrodes (symmetrically located extending from the ends of the crystal). (b) shows the trade-off in sensitivity and flatness.

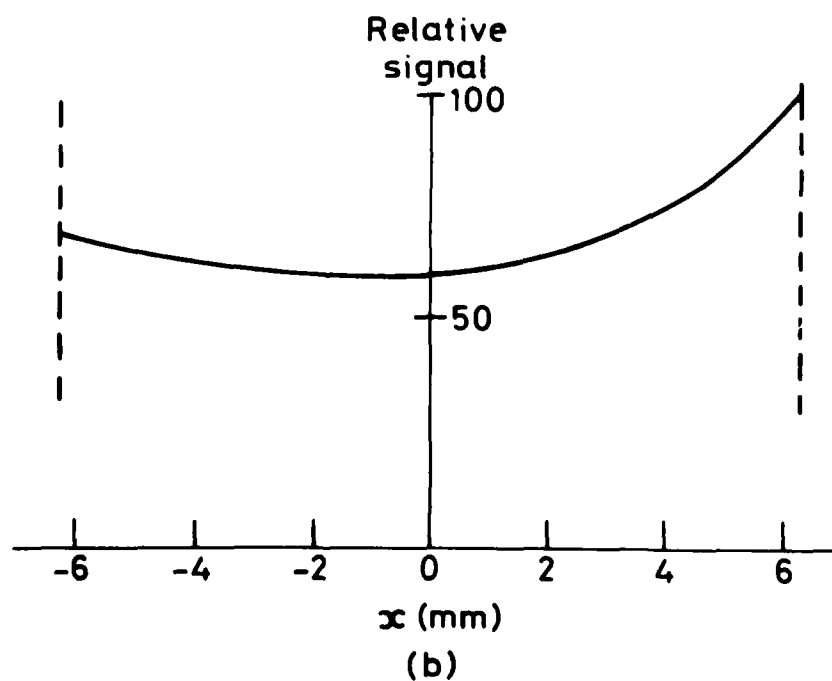
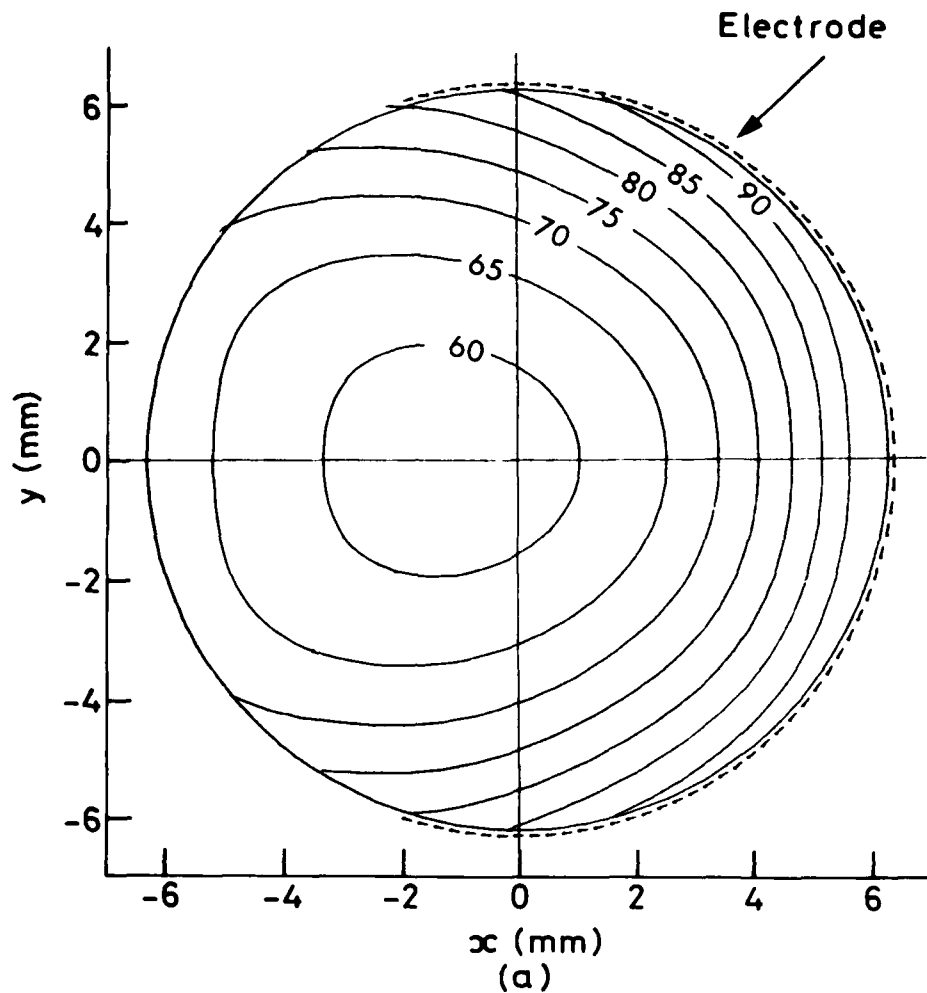


Fig.12 (a) Contour map of the response as a function of beam position for a pair of electrodes contacting 60% of the circumference. (b) Response profile along the x -axis; note the asymmetry.

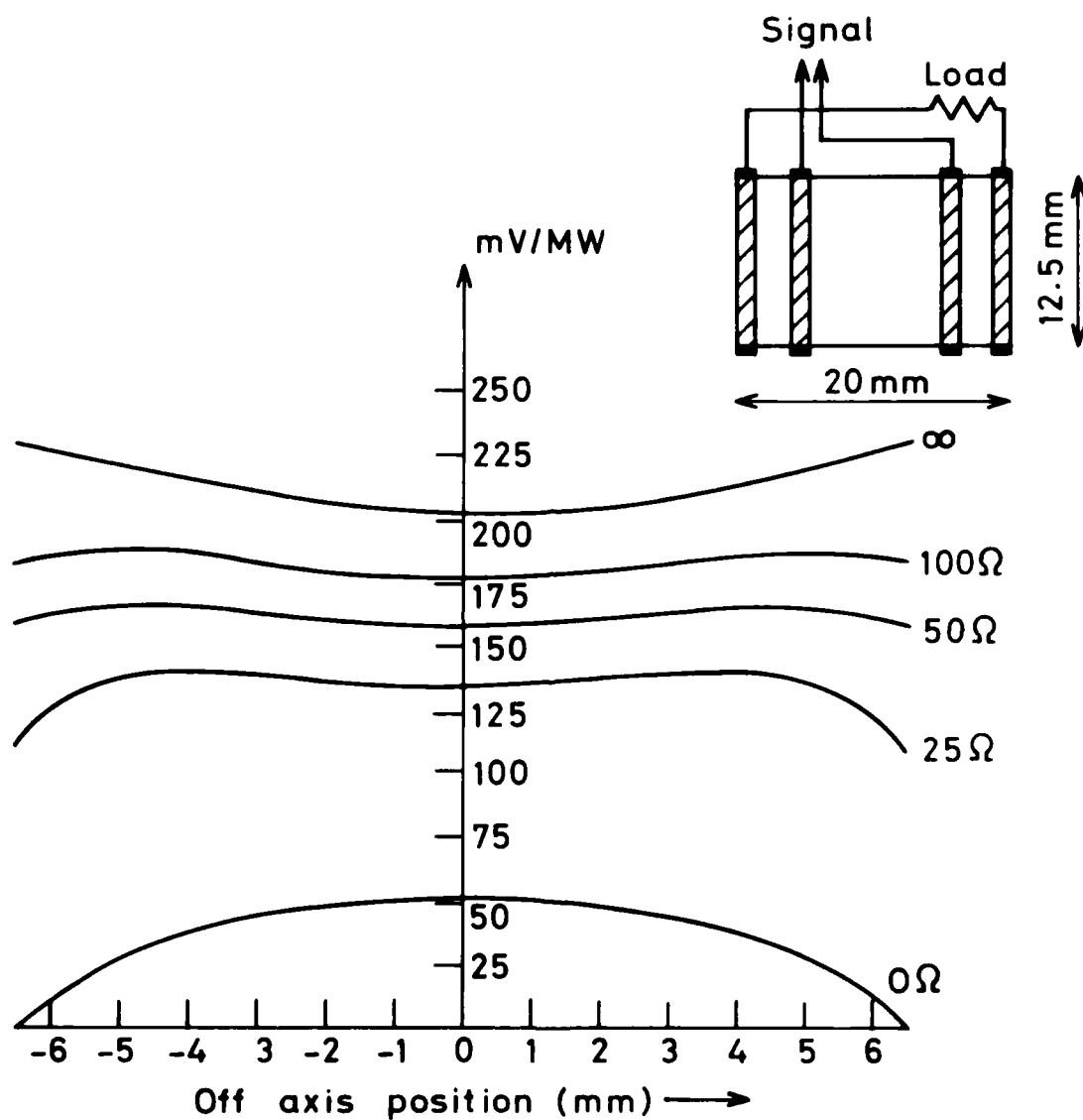


Fig.13 Schematic diagram and theoretical spatial response profiles of the 4 electrode device. The curves show the open-circuit signal generated across the inner pair of electrodes for various load resistances across the outer pair.

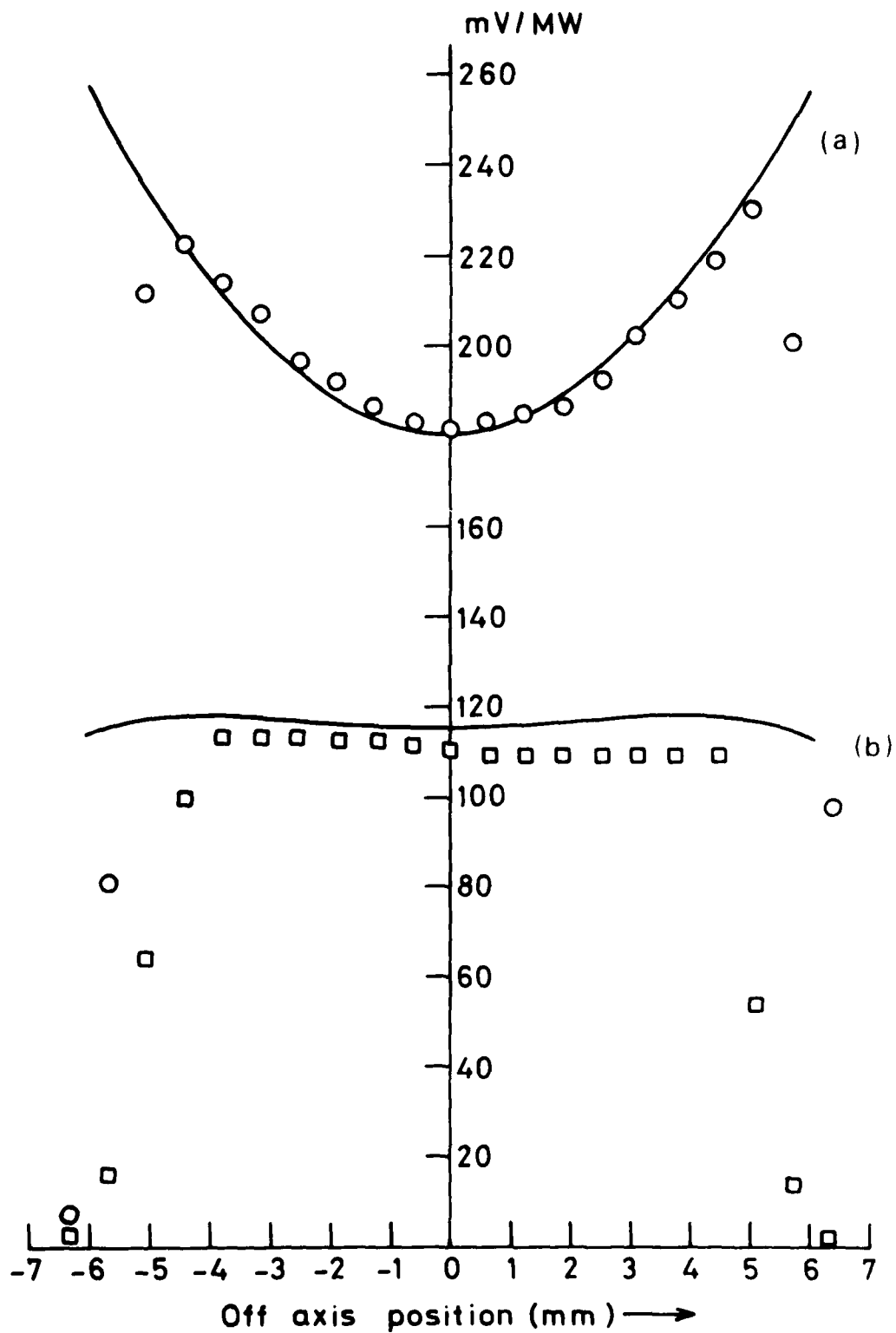


Fig.14 Theoretical (solid lines) and experimentally measured sensitivities of the 4 electrode detector as a function of beam position; (a) signal across outer pair of electrodes with inner pair isolated and (b) across inner electrodes with a $100\ \Omega$ load across the outer pair.

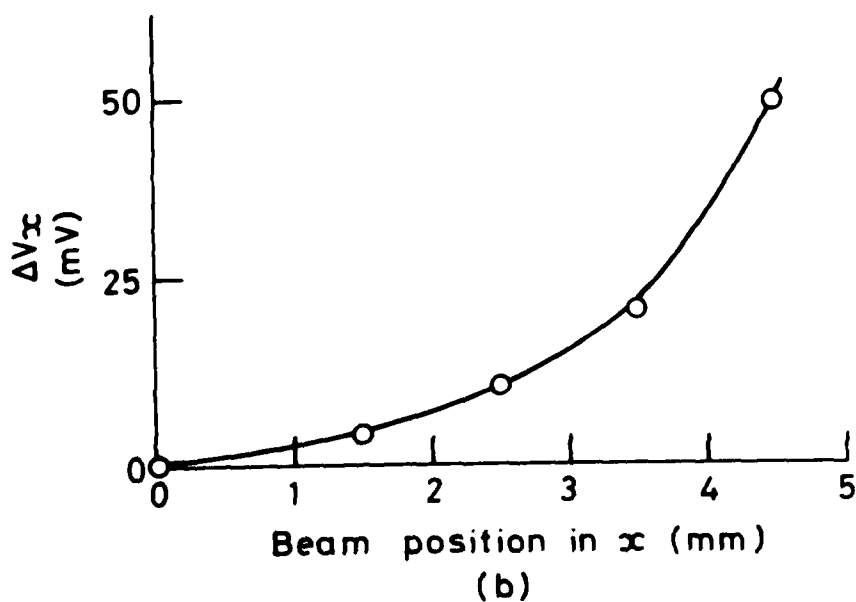
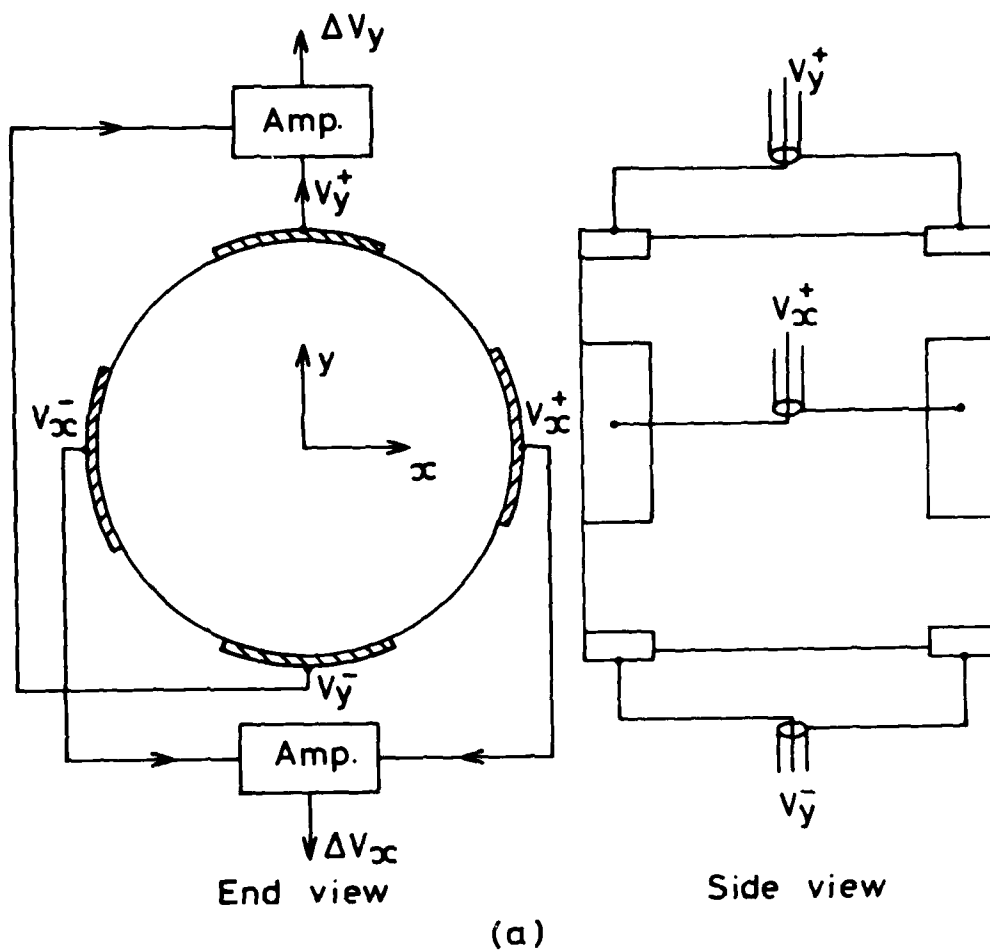


Fig.15 (a) Schematic diagram of the quadrant detector with segmented ring electrodes at each end; (b) calculated difference signal generated as the beam moves off-axis in the positive x

8 F